Continental Shelf Research 172 (2019) 33–49

Contents lists available at ScienceDirect

Continental Shelf Research

journal homepage: www.elsevier.com/locate/csr

Ocean-estuary exchange variability in a large tropical estuary

A.L. Aguiar[a,b,d,*], A. Valle-Levinson[g], M. Cirano[c,d], M. Marta-Almeida[e,f], G.C. Lessa[b], J.F. Paniagua-Arroyave[h,i]

[a] Programa de Pós Graduação em Geofísica, Universidade Federal da Bahia (UFBA), Brazil
[b] Grupo de Oceanografia Tropical (GOAT), Instituto de Física, Universidade Federal da Bahia (UFBA), Brazil
[c] Departamento de Meteorologia, Instituto de Geociências, Universidade Federal do Rio de Janeiro (UFRJ), Brazil
[d] Rede de Modelagem e Observação Oceanográfica (REMO), Brazil
[e] Centro Oceanográfico de A Coruña, Instituto Español de Oceanografía, 15001 A Coruña, Galícia, Spain
[f] Universidade de Vigo, 36310 Vigo, Spain
[g] Department of Civil and Coastal Engineering, University of Florida, 365 Weil Hall, Gainesville, FL 32611, USA
[h] Department of Geological Sciences, University of Florida, 241 Williamson Hall, Gainesville, FL 32611, USA
[i] Área de Ciencias del Mar, Universidad EAFIT, Medellín, Antioquia, Colombia

ARTICLE INFO

Keywords:
Wind-driven circulation
Lateral circulation
Nondimensional numbers
River plume
Regional modeling
ROMS

ABSTRACT

Ocean-estuary exchange variability was studied from 2008 to 2014 at a low latitude coastal plain estuary, Todos os Santos Bay, Brazil, near 13°S. Wind data from Climate Forecast System Reanalysis (CFSR) were used to complement the results of a high-resolution regional ocean model, ROMS. Volume exchange occurred under two distinct circulation patterns, namely $Circ_+$ and $Circ_-$, that matched the down-estuary (spring/summer) and up-estuary (autumn/winter) wind regimes respectively. $Circ_+$ promoted water-column stratification, while $Circ_-$ lasted longer, induced more volume exchange, and reversed the estuarine circulation. In addition, a clockwise lateral circulation (looking into the estuary) occurred during $Circ_+$, whereas a counterclockwise lateral circulation was observed during $Circ_-$. Connectivity was observed between Jaguaripe River and Todos os Santos Bay entrance. Increases in Jaguaripe River discharge, in conjunction with up-estuary winds, promoted a northward advection of the river plume toward the main entrance of the estuary, creating a lateral density gradient over Todos os Santos Bay' western shoal. Our results demonstrate that findings about estuarine circulation at higher latitudes are applicable to low latitude estuaries when dynamical depth and/or basin's width indicate that Earth's rotation is relevant.

1. Introduction

Understanding estuary-ocean exchange dynamics is of fundamental interest to estuarine research and management. Traditionally, the exchange flow is depicted as a gravitational circulation generated by an along-channel density gradient: less dense water flowing out of the bay and inflow carrying denser water from the ocean underneath (e.g., Pritchard, 1952). The structure of the gravitational circulation can be influenced by the basin's width and bathymetry (Wong, 1994; Friedrichs and Hamrick, 1996; Kasai et al., 2000; Valle-Levinson et al., 2003). Valle-Levinson (2008) investigated the density-driven exchange flow in terms of the Ekman (Ek) and Kelvin (Ke) numbers. According to this author, the exchange flow is horizontally sheared under high frictional conditions (Ek > 1) independently of the width of the basin (Ke). Under high friction, outflow occurs over the shoals, whereas inflow occupies the entire water column in the channel. The exchange pattern is also horizontally sheared under weak friction (Ek → 0) and in wide (Ke > 2) basins. However, in that case, outflow and inflow are concentrated on the left and right portion of the cross-section in the Northern Hemisphere. In the Southern Hemisphere the scenario is reversed, with outflow and inflow occupying the right and the left respectively. Moreover, under weak friction and as the width of the basin becomes small (Ke < 1), the exchange circulation tends to be more vertically sheared, with outflow at the surface and inflow underneath.

Winds are also known to modify the estuarine exchange. The influence of winds in exchange flows is mainly attributed to two processes: the remote and local wind effects. For the remote wind effect, sea level variations induced by the alongshore wind at the mouth of an estuary can produce subtidal unidirectional transport (either inflow or outflow) at the bay entrance. In contrast, the local wind effect acts directly over the surface of the estuary to produce bidirectional flow, which consists of down-wind current in the upper layer and up-wind

* Correspondence to: Grupo de Oceanografia Tropical, Universidade Federal da Bahia, Brazil.
E-mail address: aguiar.oceano@gmail.com (A.L. Aguiar).

https://doi.org/10.1016/j.csr.2018.11.001
Received 20 March 2018; Received in revised form 2 November 2018; Accepted 5 November 2018
Available online 09 November 2018
0278-4343/

current in the lower layer, with zero sectionally-integrated transport (Wong and Valle-Levinson, 2002; Guo and Valle-Levinson, 2008).

Valle-Levinson (1995) and Scully et al. (2005) demonstrated the influence of the local wind effect in the exchange pattern and estuarine stratification. Scully et al. (2005) proposed a wind straining mechanism: down-estuary wind enhances the subtidal vertical shear and strains the along-channel density gradient to increase stratification, whereas up-estuary wind reduces or even reverses the vertical shear, thus tending to decrease stratification. Chen and Sanford (2009) found that the competition between wind straining and wind mixing determines the net effect of the wind on stratification. Wind straining is accomplished by horizontal advection of fresh/dense water by wind-forced vertical shear, whereas wind mixing refers to the direct vertical mixing induced by wind stress over the water surface. Their findings suggest that moderate down-estuary winds enhance stratification, with wind straining being stronger than wind mixing. They further suggest that increased down-estuary winds promote mixing, thus reducing stratification. All up-estuary winds decrease stratification due to wind straining and wind mixing working in concert. Regarding the lateral circulation induced by the wind, Li and Li (2011) found that in the presence of rotational effects (considering the Northern Hemisphere), the down-estuary and up-estuary winds drive counterclockwise and clockwise circulations, which steepen and flatten isopycnals in cross-channel sections respectively, and reduce vertical shear in the along-channel currents.

Several studies have explored along-estuary flows at mid (~25° to ~60°) and high (> 60°) latitudes (e.g., Valle-Levinson et al., 1998; Ponte et al., 2012; Inall et al., 2015). However, the literature about estuarine circulation in low latitudes is scarce (e.g., Smeed, 2004; Amorim et al., 2011; Valle-Levinson and Schettini, 2016; Santana et al., 2018) and leaves open questions. For example, how do results from higher latitudes apply to estuaries close to the Equator? What should be considered to study the exchange flow in low latitude estuaries? Although an extensive knowledge has been amassed on estuarine exchange, most of the relevant studies were based on spatially and temporally limited observational surveys (e.g., Valle-Levinson et al., 2001), short-term model simulations (e.g., Guo and Valle-Levinson, 2007), or isolated events (e.g., Valle-Levinson et al., 2002). Hence, the present work has the main purpose of evaluating the estuary-ocean exchange dynamics based on a long-term (7 years) realistic model simulation at a low latitude (13°S) estuary.

1.1. Regional setting

The Todos os Santos Bay (Fig. 1d) is the second largest Brazilian bay, centered on latitude 12° 50'S and longitude 38° 30'W, and with an approximate maximum width (west-east axis) and length (north-south axis) of 32 km and 50 km respectively. The bay is a typical coastal plain estuarine system that receives the discharge of the three major drainage basins of the Paraguaçu, Subaé and Jaguaripe rivers. Its maximum area and wet perimeter at an equinoctial spring tides correspond to 1223 km^2 and 1175 km respectively. The Todos os Santos Bay has an area-weighted depth of 9.8 m. Approximately 94% of its area is shallower than 25 m. The intertidal area is 327 km^2 (27%), where 152 km^2 are occupied by mangroves and 175 km^2 by non-vegetated flats. The volume of the bay during maximum spring tides is approximately 12×10^9 m^3, whereas the volume below the hydrographic datum is 8.9×10^9 m^3, thus generating a maximum spring-tidal prism of approximately 3.1×10^9 m^3 (Cirano and Lessa, 2007).

Tides are semi-diurnal, with form number ≤ 0.11. Upon entering the bay, the tidal wave is progressively amplified and distorted, especially in the narrow, winding and/or shallow regions. In the most internal part of the bay, the form number can reach 0.06. The estuary has a meso-tidal regime and tidal ranges increase up bay by a factor of 1.5. M_2 amplitude grows from 0.67 m in the ocean to 0.89 m in the center of the bay, 0.93 m in the bay's northern cove and Canal de Itaparica and 1.06 m at Baía de Iguape (Fig. 1d). In the central axis of the bay, 97.5% of the variance in water level is due to the action of the astronomical tide, and within the bay 86% of the variance of the currents is controlled by the tidal regime (Cirano and Lessa, 2007). Xavier (2002) noted variations in currents between neap and spring tides (when the currents are 50% more intense), however no variation was found between summer and winter. Based on drifter data, tidal excursion values fall between 3.7 and 7 km, adopting the value of 6 km as standard for the bay.

The wind regime in the region is determined by seasonal trade winds. During the spring/summer, winds blow preferentially from the NE. During autumn/winter, however, winds blow from the E/SE when

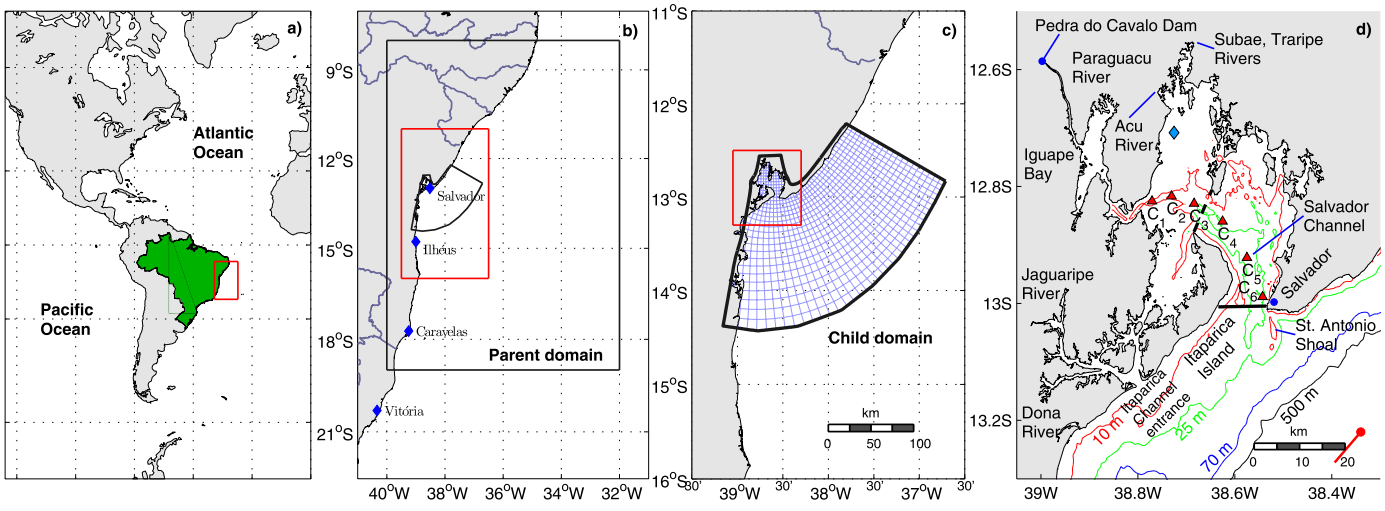

Fig. 1. Model domain (a to c) and bathymetry of the study region (d). Panels b) and c) illustrate the parent and child domains. The blue diamonds in panel b) indicate the INPE meteorological stations where cold front passages were recorded. In panel c), the child domain grid was plotted in intervals of 10 grid lines to improve visibility. In panel d), the solid black line indicates the cross-section to estimate the exchange flow at the bay entrance. The dashed black line (around C_3) indicates the inner bay section to estimate the horizontal density gradient across the bay. The light blue diamond indicates the inner point of the bay to compute the differences in the sea level between the entrance and inner bay. The CTD hydrographic stations are represented by red triangles (C_1-C_6). The red dot and red line indicate the grid point and the orientation adopted to estimate Ekman transport respectively. The 10 (red), 25 (green), 70 (blue) and 500 m (black) isobaths are represented. The red rectangles in panels a) to c) correspond do the areas of the panels b) to d). (For interpretation of the references to color in this figure legend, the reader is referred to the web version of this article).

the passage of cold fronts is frequent (Dominguez, 2006).

The water balance at the bay entrance is positive over most of the year, i.e., export from the estuary. Pluvial precipitation concentrates from March to July, when 60% of the annual mean precipitation occurs. In the mainland, however, the monthly distribution of rainfall is out of phase with that over the bay. For example, the wet season occurs between November and February in the mainland (Cirano and Lessa, 2007).

The river inflow within the bay is dominated by the Paraguaçu River, with the mean discharge of 92.5 m^3s^{-1} between 1947 and 2003. However, Paraguaçu discharge has been regulated by the Pedra do Cavalo Dam since 1986 (Fig. 1d). Additionally, Jaguaripe and Subaé rivers contribute with average flow rates of 9 and 4.8 m^3s^{-1}, respectively (Lessa et al., 2009). Local differences in precipitation produce an alternate seasonality relative to riverine water input into the bay. The Paraguaçu River discharge depends on precipitation over land. Rainfall over the bay feed Subaé and Jaguaripe rivers, and coastal streams. Thus, Paraguaçu River peaks from November to February (austral summer), whereas other rivers peak from April to June (austral autumn). Nevertheless, Jaguaripe River does not effectively contribute to the freshwater inflow to Todos os Santos Bay because it discharges to the Atlantic Ocean, south of Itaparica island (Xavier, 2002).

Xavier (2002) investigated the residual circulation using a barotropic circulation model (SisBAHIA). This author suggested the dominance of ebb in most of the bay, while some regions where flood dominates would induce the formation of vortices resulting from nonlinear interactions between the tidal flow and bathymetry. Cirano and Lessa (2007), based on in situ data from the Bahia Azul Program (CRA, 2001), identified currents with opposite directions at the bottom and surface (gravitational circulation) at the bay entrance and inner bay, both in the summer and in the winter. Santana et al. (2018) studied the seasonality of the residual circulation at the bay entrance and their forcings using the Regional Ocean Modeling System (ROMS). Their simulation was started under barotropic conditions and used climatological forcing, except tidal forcing. Their results indicated that the residual circulation is mainly driven by tides, followed by river discharge, with an inflow in the channel center and outflow on the shoulders.

2. Data and methods

2.1. Model setup

Simulations of ocean-estuary exchange were performed using ROMS (Shchepetkin and McWilliams, 2005; Haidvogel et al., 2008). ROMS is a three-dimensional model that solves the free surface, hydrostatic, primitive equations of the ocean over variable bathymetry. In addition, ROMS is highly configurable for use in realistic regional applications. The model horizontal domain resolution is variable, being 300–400 m inside the bay and 600–1200 m at the open boundaries. The vertical direction was discretized with 32 sigma-levels of increased resolution toward the surface. The bathymetry was interpolated from a blend of ETOPO (Amante and Eakins, 2009) and very high resolution measurements taken by the Brazilian Navy.

Model outputs were analyzed as daily averages and hourly snapshots. Hourly snapshots were calculated in approximately 2000 points (stations) distributed within the model domain. Daily outputs were used to study the ocean-estuary exchange flow. Hourly snapshots were not used in this task due to interpolation errors in the generation of the stations output. While these errors are very small, less than 0.1% in the cross-section transports at each hourly output, they propagate in time so that after days and months they become non-negligible. Nevertheless, hourly outputs were used to identify spring and neap tide peaks and to estimate the tidal current amplitude.

Atmospheric fluxes were taken from the Climate Forecast System Reanalysis (CFSR) (Saha et al., 2010), which belongs to the new generation of reanalysis being more accurate than the previous datasets from the National Centers for Environmental Prediction (NCEP), particularly in the Southern Hemisphere. The surface variables of CFSR are available at a spatial resolution of 0.3° with a time interval of 6 h.

Tidal forcing was imposed at the model open boundaries. The tidal data were obtained from the TPXO 7.1 global database (Egbert and Erofeeva, 2002), which provided the amplitudes and phases of the sea surface elevation and barotropic currents for the eight primary constituents (M_2, S_2, N_2, K_2, K_1, O_1, P_1, Q_1), obtained from the 1/12° Regional Atlantic Ocean-ATLAS solution; and the two long-period constituents (M_f, M_m), obtained from the 1/4° Global Ocean-ATLAS solution. Shallow-water frequencies provided by the datasets were excluded. These frequencies are generated by the model as the tidal wave interacts with shelf and bay bathymetries.

Riverine inputs were incorporated as daily values for the rivers and monthly values for the coastal streams. Data sources and methodologies used to obtain the discharges were: Paraguaçu River was measured at the Pedra do Cavalo Dam; Subaé and Jaguaripe rivers were measured by ANA (Portuguese acronym for National Water Agency); Traripe and Açu rivers were estimated based on Subaé River; Dona River was estimated based on Jaguaripe River; and the coastal streams monthly values were estimated from precipitation and historical data. The estimations followed CRA (2001). The rivers were introduced in the model at the river mouth while the coastal streams were distributed by eight locations around the bay. River temperatures were set as equal to the climatological surface air temperature for the region from da Silva et al. (1994).

This work used seven years of simulation results from the beginning of 2008 until the end of 2014, using initial and boundary conditions, through offline nesting, from a regional parent model with horizontal resolution 1/36° based on Amorim et al. (2013). This parent model was developed under the framework of the Oceanographic Modeling and Observation Network (REMO, Lima et al., 2013) for the region between 8°S to 19°S and 32°W to 40°W including the Eastern Brazilian Shelf and the adjacent deep ocean (Fig. 1b). The vertical resolution consisted of 32 sigma-levels. The surface and tidal forcing were the same as used in this work. Lateral forcing was obtained from the Hybrid Coordinate Ocean Model coupled with the Navy Coupled Ocean Data Assimilation (HYCOM/NCODA, HYCOM, 2011) as daily values having horizontal resolution of 1/12°. The 5-day average outputs of this parent model were used on the offline nesting. The nesting followed the approach tested by Marta-Almeida et al. (2013). Further details about the model configuration and model validation against observations are given in Marta-Almeida et al. (2017, 2018). The validation showed the model ability to reproduce the thermohaline field, tidal currents and the variability of the free surface at tidal and sub-tidal time scales.

This shelf-estuary configuration is an evolution of the previous ROMS modeling studies in the region, such as works focused on upwelling processes (Aguiar et al., 2014, 2018), operational modeling (Marta-Almeida et al., 2011a, 2011b), oil dispersion (Marta-Almeida et al., 2013) and shelf circulation (Amorim et al., 2013). This model configuration also represents an improvement compared to previous modeling studies in Todos os Santos Bay, e.g., Santana et al. (2018), whose experiments were based on homogeneous initial conditions and climatological forcing. Hence, this study is the first attempt to understand the exchange flow dynamics in the bay using realistic simulations.

2.2. Identification of exchange pulses

To remove the main tidal signals, the model outputs were filtered using a low-pass Lanczos filter of 60 h, as the inertial period in the region is about 53 h. The subinertial band, however, includes not only the variability relative to exchange pulses but also the tidally rectified current and gravitational circulation. Thus, to isolate the effect of the exchange pulses, a Singular Spectrum Analysis algorithm (SSA) (Marques et al., 2006) was used to decompose the filtered results into a background slowly varying trend (tidally rectified current and

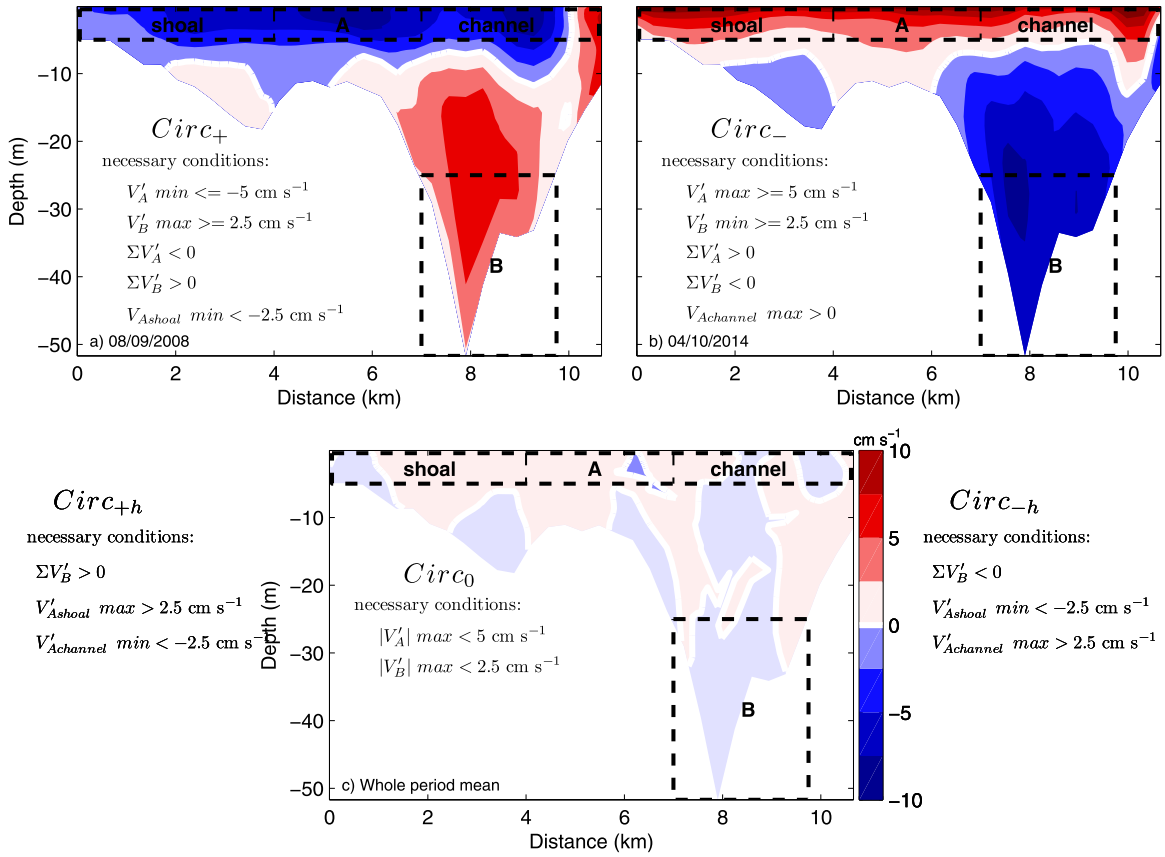

Fig. 2. Representation of exchange circulation patterns and their necessary conditions at the cross-section at the bay entrance illustrated in Fig. 1d. The thick dashed lines indicate the sectors, namely A and B, while thin dashed lines indicate the A_{shoal} and $A_{channel}$ divisions within sector A. Positive and negative velocity anomaly values indicate inflow and outflow respectively. The white solid line indicates the level of no motion. $Circ_0$ represents the mean subinertial circulation, i.e., a circulation scenario where no exchange pulses occur. The interval between isotachs is 2.5 cm s^{-1}. The x-axis indicates the distance in km from the western margin of the bay entrance.

gravitational circulation) and corresponding anomaly (variability induced by exchange pulses). The SSA was performed with a window length of 20 elements and the first three eigentriples were used to reconstruct the background low frequency. Hereafter, synoptic exchange flow refers to the exchange flow anomaly, whereas total exchange flow refers to the entire subinertial band of the flow (fortnightly + synoptic variability).

We consider "exchange pulses" as the strengthening, weakening or reversing of the mean gravitational circulation. Thus, such pulses represent anomalies to the exchange flow, inducing more or less horizontally sheared flow or a vertically sheared flow at the bay entrance. The following four circulation scenarios were then established: intensification and attenuation/reversal of the vertically sheared gravitational circulation ($Circ_+$ and $Circ_-$); and intensification and attenuation/reversal of the horizontally sheared gravitational circulation ($Circ_{+h}$ and $Circ_{-h}$).

An automatic method was developed to identify each circulation pattern based on the criteria described as follows. The water column at the bay entrance was divided in 2 sectors (Fig. 2): A and B, which correspond to the surface layer (0–5 m) and deep channel (25 m to the bottom) respectively. In addition, sector A comprises 2 subsectors: A_{shoal} and $A_{channel}$, which represent the part of the surface layer over the shoal (0–4 km from the western margin) and over the deep channel (7 km from the western margin to the eastern margin). $Circ_+$ has as necessary conditions: i) the average along-channel velocity anomaly to be negative (outflow) in A and positive (inflow) in B; ii) the strongest outflow velocity anomaly to be greater than 5 cm s^{-1} in A and the strongest inflow velocity anomaly to be greater than 2.5 cm s^{-1} in B; and iii) the strongest outflow velocity to be greater than 2.5 cm s^{-1} in A_{shoal}. $Circ_-$ has as necessary conditions: i) the average along-channel velocity anomaly to be positive in A and negative in B; ii) the strongest inflow velocity anomaly to be greater than 5 cm s^{-1} in A and the strongest outflow velocity anomaly to be greater than 2.5 cm s^{-1} in B; and iii) the strongest inflow velocity to be greater than 2.5 cm s^{-1} in $A_{channel}$. $Circ_{+h}$ requires: i) the average along-channel velocity anomaly to be positive in B; ii) the strongest inflow and outflow velocity anomalies to be greater than 2.5 cm s^{-1} in A_{shoal} and $A_{channel}$ respectively. $Circ_{-h}$ requires: i) the average along-channel velocity anomaly to be positive in B; and ii) the strongest outflow and inflow velocity anomalies to be greater than 2.5 cm s^{-1} in A_{shoal} and $A_{channel}$ respectively. As neither $Circ_{+h}$ nor $Circ_{-h}$ were identified in the model outputs, only $Circ_+$ and $Circ_-$ were investigated. The peak of an exchange pulse was considered when the highest outflow and inflow velocity occurred in $A_{channel}$ among contiguous $Circ_+$ and $Circ_-$ respectively. In addition, the start and end dates for each pulse were also identified. A $Circ_+$ pulse lasts as outflow velocities > 2.5 cm s^{-1} appear over A_{shoal} preceding and succeeding a $Circ_+$ peak. Analogously, a $Circ_-$ pulse lasts as inflow velocities are found in $A_{channel}$ preceding and succeeding a $Circ_-$ peak.

2.3. Analysis of exchange mechanisms

To evaluate exchange pulses, the synoptic exchange flow was divided into barotropic and baroclinic, represented by the unidirectional (Q_{Uni}) and bidirectional (Q_{Bi}) components of the flow respectively. This procedure followed Wong and Valle-Levinson (2002):

$$\begin{aligned} Q_{Uni} &= Q_{in} + Q_{out} \\ Q_{Bi_{in}} &= Q_{in} - (1-A_{out})(Q_{Uni}) \\ Q_{Bi_{out}} &= Q_{out} - (A_{out})(Q_{Uni}) \end{aligned} \quad (1)$$

where Q_{net} is the sectionally integrated subinertial net flux; Q_{in} (positive) and Q_{out} (negative) are the flux in and out of the bay, respectively; A_{out} represents the fractional area of the cross-section that carries outflow; and $Q_{Bi_{in}}$ and $Q_{Bi_{out}}$ indicate the inflow and outflow components of Q_{Bi}. The along-channel velocity anomalies were used to estimate the volume fluxes in Eq. (1). Regarding the net exchange through the bay entrance, only Q_{Uni} contributes to the sectionally integrated volume flux, since $Q_{Bi_{in}} + Q_{Bi_{out}} = 0$. Wong and Valle-Levinson (2002) isolated the wind-induced flow by removing the tidally rectified current and the gravitational circulation. In the present work, however, we consider that synoptic exchange flows include the exchange flows driven by river discharge pulses in the region. Therefore, the components of the flow are called unidirectional and bidirectional instead of remote (Q_R) and local (Q_L) wind effects as in Wong and Valle-Levinson (2002). Furthermore, the components of the flow were used as a reference to classify exchange pulses in four ranks of intensity: std_0 to std_3. Beforehand, we verified whether Q_{Uni} or Q_{Bi} dominated during the pulse peak. Then, each pulse was classified according to the dominant component of the synoptic exchange flow. When Q_{Bi} was dominant over Q_{Uni}, the pulse was considered: std_0 if Q_{Bi} was below 1 standard deviation; std_1 if Q_{Bi} was between 1 and 2 standard deviations; std_2 if Q_{Bi} was between 2 and 3 standard deviations; and std_3 if Q_{Bi} was above 3 standard deviations during the pulse peak.

Ekman transport (T_{ek}) was estimated to evaluate the influence of the alongshore wind on Q_{Uni}. The estimates of T_{ek} (in units of $m^3 s^{-1}$ per meter of coast) were obtained using the Smith (1968) formulation: $T_{ek} = \vec{\tau} . \hat{t}/\rho_o f$, where $\vec{\tau}$ is the wind stress vector; $\hat{t}$ is a unit vector tangent to the local coastline ($\hat{t}$ direction is indicated by the red line in Fig. 1d); ρ_o is the reference water density (1024 kg m^{-3}); and f is the Coriolis parameter. T_{ek} was estimated considering a grid point 40 km from the coast, as indicated in Fig. 1d. A similar methodology was used by Aguiar et al. (2018).

To investigate the balance of the forces and their effects on the subinertial circulation, the following nondimensional numbers were estimated. The importance of rotational effects on density-induced or wind-induced water exchange can be evaluated by Ke and Ek (e.g., Kasai et al., 2000; Valle-Levinson, 2008; Li and Li, 2011). Ke compares the basin's width to the internal Rossby radius (Rd_i), as shown in the equation below:

$$\begin{aligned} Ke &= \frac{B}{Rd_i} \\ Rd_i &= \frac{\sqrt{g' h_S}}{f} \\ g' &= g\left(\frac{\Delta\rho}{\rho_o}\right) \end{aligned} \quad (2)$$

where B is the basin's width, h_S is the depth of the surface layer containing the buoyant part of the density-induced flow, g' is the reduced gravity, g is the gravity acceleration and $\Delta\rho$ is the density difference between the surface and bottom layers. h_S was estimated as the average depth of the no motion isotach (subinertial velocity = 0 m s^{-1}) that separates the surface and bottom flows considering 7 km from the western margin to the eastern margin. $\Delta\rho$ was calculated as the difference of the average subinertial density in $A_{channel}$ and that in sector B. Ke > 1 implies that the basin's width is larger than Rd_i, thus Earth's rotation effects are supposed to be relevant.

Ek evaluates whether the Coriolis or frictional effects dominate ($Ek = A_z/fH_{max}^2$, where A_z is the sectionally averaged vertical eddy viscosity and H_{max} is the channel's maximum depth). Earth's rotation effects become negligible when Ek > 1.

To infer the mechanism responsible for the total exchange flow, three nondimensional numbers were estimated: Wedderburn (Wn), Stress ratio (S_0) and tidal Froude numbers (Fr_0). We can gauge the relative importance of the wind against the horizontal density gradient forcing by calculating Wn (Monismith, 1986; Geyer, 1997; Chen and Sanford, 2009; Li and Li, 2011);

$$Wn = \frac{\tau_W L}{\Delta\rho_h g H^2} \quad (3)$$

S_0 (Tenorio et al., 2018) indicates whether tidal ($S_0 > 1$) or wind ($S_0 < 1$) stresses dominate to drive the total exchange flow;

$$S_0 = \frac{U_o^2 \rho_o H}{\tau_W L} \quad (4)$$

and Fr_0 (Valle-Levinson and Schettini, 2016) assigns whether tidal stress ($Fr_0 > 1$) or baroclinicity ($Fr_0 < 1$) is more important;

$$Fr_0 = \frac{U_o^2 \rho_o}{\Delta\rho_h g H} \quad (5)$$

where U_o is the tidal current amplitude, τ_W is the sectionally averaged along-channel wind stress, L is the length of the estuary, $\Delta\rho_h$ is the horizontal density difference, and H is the estuary mean water depth. Based on model bathymetry, H is about 10 m. To estimate U_o, tidal current amplitude was obtained applying harmonic analysis to model hourly outputs and considering 68 tidal constants (t-tide, Pawlowicz et al., 2002). Then the maximum absolute along-channel tidal current was calculated for each day. These daily values were sectionally averaged to obtain the mean tidal current amplitude at the bay entrance for each day. $\Delta\rho_h$ was estimated as the difference between the sectionally averaged density at the bay entrance and at the inner channel over the distance L as illustrated in Fig. 1d.

Finally, to quantify the stratification at the bay entrance, the Richardson number was estimated as follows:

$$Ri = \frac{-\frac{g}{\rho_o}\frac{\partial\rho}{\partial z}}{\left(\frac{\partial u}{\partial z}\right)^2 + \left(\frac{\partial v}{\partial z}\right)^2} \quad (6)$$

where u and v are the cross-channel and along-channel components of the velocity respectively. The Richardson number compares stratification to mixing so that if Ri > 0.25 the water column is considered stratified.

3. Results

3.1. Thermohaline validation

The thermohaline validation of the model inside the bay was based on temperature and salinity profile data collected along the main axis of the bay (Fig. 1d). These data were provided by a recent observational State-financed project named Kirimurê. The observations were obtained between May 2012 and June 2014 once/twice per month in a total of 39 campaigns, during the extremes of spring and neap tides. The profiles were measured from the bay entrance to the Paraguaçu River mouth following the tidal wave. The model output was stored every 15 min and the records closest in time to the observations were used for the comparison.

The agreement between model and observations is quantified in Table 1, which includes the RMSE and correlation coefficients at each station for the vertically averaged values and for the upper, middle and bottom layers (each corresponding to one third of the water column). Table 1 shows correlation coefficients mostly higher than 0.95 and 0.90 for temperature and salinity respectively. The highest correlations are found at the western side of the bay (C_1, C_2 and C_3). At the bay entrance (C_6), these values are a bit lower, but still higher than 0.90. In terms of RMSE values, those are typically around 0.6 °C for temperature. The

Table 1
RMSE and correlation coefficients between model results and observations for the vertically averaged values (bar) and for the upper, middle and bottom layers (each corresponding to one third of the water column) at sites C_1 to C_6, as indicated in Fig. 1b. Errors lower than 0.5 and higher or equal to 0.75 are highlighted (bold and italic respectively). In the same way, correlation coefficients higher or equal to 0.95 and lower than 0.90 are also highlighted in bold and italic respectively.

		Temperature (°C)						Salinity (g kg^{-1})					
		C_1	C_2	C_3	C_4	C_5	C_6	C_1	C_2	C_3	C_4	C_5	C_6
RMSE	bar	*0.76*	0.62	0.65	0.66	**0.44**	0.55	0.61	**0.47**	**0.36**	**0.42**	**0.40**	**0.24**
	top	0.65	**0.49**	0.56	0.63	**0.47**	0.60	*0.85*	0.68	0.57	0.52	0.50	**0.26**
	middle	*0.78*	0.66	0.67	0.67	**0.45**	0.55	0.53	**0.43**	**0.32**	**0.41**	**0.39**	**0.23**
	bottom	*0.89*	*0.78*	*0.75*	0.70	**0.44**	0.54	0.52	**0.39**	**0.24**	**0.35**	**0.32**	**0.22**
Corr coef	bar	**0.97**	**0.98**	**0.99**	**0.97**	**0.95**	0.92	0.93	0.93	**0.95**	0.92	0.92	0.92
	top	**0.97**	**0.98**	**0.98**	**0.97**	0.93	0.91	*0.89*	*0.89*	0.92	0.90	0.90	0.90
	middle	**0.97**	**0.98**	**0.98**	**0.97**	**0.95**	0.92	**0.95**	0.94	**0.96**	0.92	0.92	0.92
	bottom	**0.97**	**0.97**	**0.98**	**0.98**	**0.96**	0.92	0.94	**0.95**	**0.97**	0.93	0.92	0.92

RMSE salinity values are mostly lower than 0.5 g kg^{-1}. In C_1, salinity RMSE is 0.85 g kg^{-1} in the first third of the water column, probably because it is the station closer to the Paraguaçu river mouth. Conversely, the lowest salinity errors are found at the bay entrance (C_6). Considering the three portions of the water column, RMSE and correlation coefficients show that the model results achieve a good representability of observed data throughout the water column.

3.2. Mean subinertial circulation

Fig. 3 shows the wavelet analysis for the total exchange flow and its forcings during the 2008–2014 period. The exchange flow at the bay entrance is mainly associated to tidal fortnightly variability as the maximum amplitudes occur around 15-day periods (Fig. 3a). Figs. 3b and c indicate that Ekman transport and along-channel wind stress have a similar pattern, with higher amplitudes occurring at annual periods. The water balance (E-P) exhibits a marked annual cycle as well (Fig. 3d), which corresponds to the dry and wet (rainy) seasons in the region as indicated by Cirano and Lessa (2007). The total river discharge (which takes into account all rivers, except Jaguaripe and Dona rivers, and coastal streams) reveals higher amplitudes at 1–2 monthly cycles (Fig. 3e) during December and January, which is closely related to the seasonal peaks of Paraguaçu River. Only in 2010 an energy peak at the annual period occurs, which may indicate interannual variability as this peak does not include the other years. In fact, Paraguaçu discharges were almost null in 2012 and 2013. Hence, exchange flow

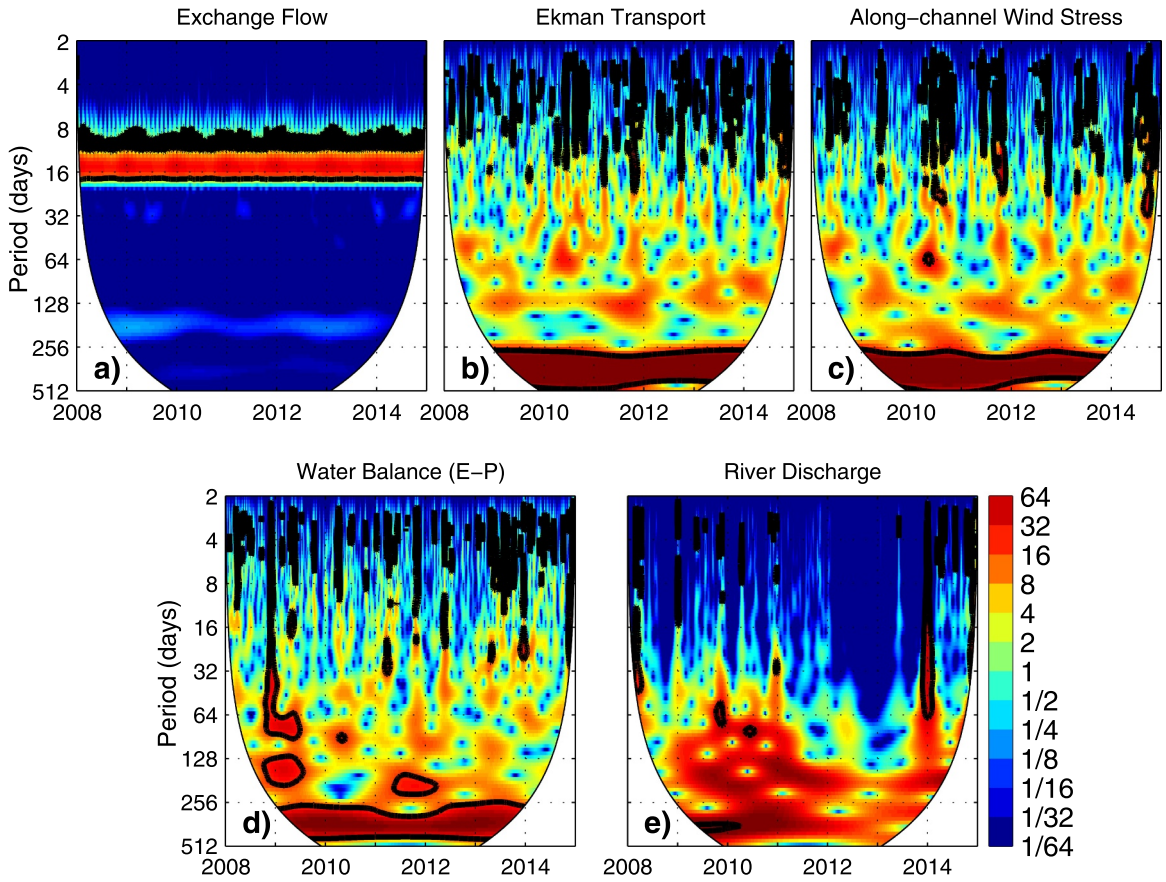

Fig. 3. Wavelet transforms of a) subinertial exchange flow at the cross-section at the bay entrance (Fig. 1d) and its forcings: b) Ekman transport, c) along-channel wind stress, d) water balance (evaporation minus precipitation), and e) river discharge. The black thick line encloses regions with statistical significance at the 95% level of confidence. The white shade indicates the "cone of influence", where edge effects become important. The wavelet package was provided by Aslak Grinsted (see Grinsted et al. (2004)).

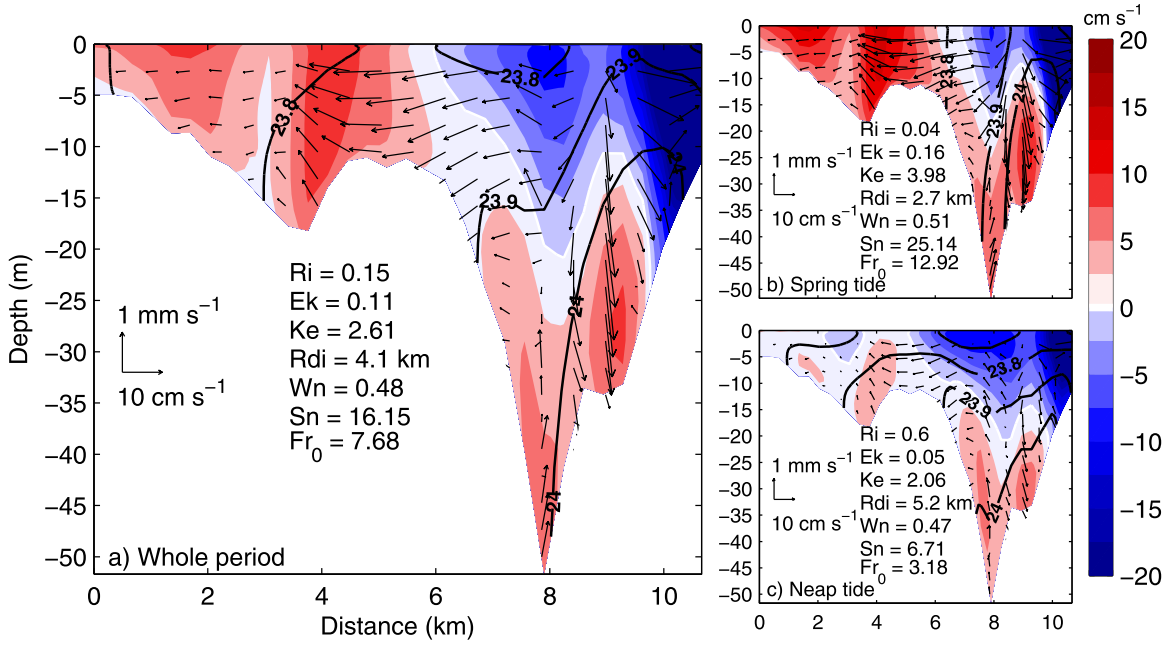

Fig. 4. Mean subinertial circulation at the cross-section at the bay entrance (Fig. 1d) considering a) the whole period (2008–2014), b) spring tide peaks, and c) neap tide peaks. Positive and negative values indicate inflow and outflow respectively. Vectors represent the lateral circulation. Solid lines indicate isypicnal contours. Nondimensional numbers and internal radius of deformation mean values are indicated. The interval between isotachs is 2.5 cm s^{-1}. The x-axis indicates the distance in km from the western margin of the bay entrance.

exhibits a fortnightly variability mainly related to tides. Other forcings show a marked annual variability, mostly associated with austral summer-winter cycles, and interannual variability in riverine discharge.

Fig. 4 presents the 7-year mean exchange flow at the bay entrance and the mean exchange flow during spring and neap tide peaks. Spring and neap tide peaks were identified using model hourly outputs at a point (station) in the middle of the bay entrance. Thus, a spring peak was considered as the day when the highest sea level amplitude was observed during spring tides. Analogously, a neap peak was considered as the day when the lowest sea level amplitude was observed during neap tides. The mean circulation reveals a horizontally sheared exchange, with denser water entering the bay through the deep channel and over the shoal, whereas the outflow is restricted to the upper layer in the main channel. Laterally, the cross-channel flows at the surface moves to the left of the outflow, and the lateral flow at the layer underneath moves to the left of the inflow. According to previous studies (e.g., Kasai et al., 2000; Valle-Levinson et al., 2003; Valle-Levinson, 2008), this circulation pattern corresponds to a dynamic regime where Earth's rotation effect is important and dominates over friction. Thus, to verify that assumption, nondimensional numbers were estimated for each profile shown in Fig. 4. In fact, Ekman (0.11) and Kelvin (2.61) numbers corroborate that rotation effect prevails over friction. The exchange flow structure shown in Fig. 4a resembles that of Fig. 5a in Valle-Levinson (2008), with a similar Ke but an Ek three orders of magnitude larger compared to this author's findings.

During spring tides (Fig. 4b), the mean circulation is very similar to that depicted in Fig. 4a, but with few distinct features. Spring tides showed more vigorous exchange flow than the mean and more vertical homogeneity in the density field (Fig. 4b). This enhanced mixing causes the internal radius of deformation to be 1.4 km smaller, which in turn constrains the outflow more to the right compared the mean scenario. Hence the mean exchange tends to be more horizontally sheared, being more similar to Fig. 5a in Valle-Levinson (2008) (Ke = 4), as Ke increased to 3.98. During neap tides (Fig. 4c), weaker exchange flows occur under increased stratification (Ri = 0.6). Todos os Santos Bay shifts from a well-mixed to a partially mixed regime. As a consequence, the internal Rossby radius increases to 5.2 km, Ke decreases to 2.06, and the outflow occupies most of the surface layer. The structure of along-channel flows during neap tide reveals increased vertically sheared flows and thus resembles that depicted in Fig. 5d in Valle-Levinson (2008) with Ek = 0.0002 and Ke = 1. With regard to the forcing of total exchange flow at Todos os Santos Bay, tidal rectification dominated over gravitational circulation ($Fr_0 > 1$), which, in turn, dominated over wind stress ($S_0 > 1$) regardless of the tides. This result is consistent with Santana et al. (2018), who demonstrated that the residual circulation at the bay entrance is mainly tidally driven, with baroclinicity playing a secondary role. On the other hand, this result is different from those found by Valle-Levinson and Schettini (2016) in a Brazilian tropical estuary (~5°S), where tidal rectification prevails during spring tides, whereas baroclinicity dominates during neap tides.

3.3. Ocean-estuary exchange pulses

The time series of Q_{Uni} and Q_{Bi} during the 2008–2014 period are linked to exchange pulses and cold frontal passages (INPE, 2017) (Fig. 5). The unidirectional exchange flow (black line) induced by wind and/or density gradient pulses reaches up to approximately 1800 m^3s^{-1}. The bidirectional exchange flow (gray line) is stronger than Q_{Uni}, with transport values reaching 2500 m^3s^{-1}. However, neither $Q_{Bi_{in}}$ nor $Q_{Bi_{out}}$ contribute to any volume exchange, as their sum is null. Wong and Valle-Levinson (2002) suggest that these transports may impact the exchange of dissolved and suspended material between the estuary and the coastal ocean. This is because the distribution of the waterborne material in the outflow may be different from that in the inflow. The exchange pulses exhibit a clear seasonality, with $Circ_+$ occurring preferentially from September to March while $Circ_-$ occurs from April to August (Fig. 5). This pattern resembles wind seasonality in the region (Fig. 6a to d). $Circ_+$ pulses were more frequent during the spring/summer period, when the wind was preferentially from the E/NE. In contrast, $Circ_-$ pulses were more likely to occur during S/SE winds, which were more frequent during the autumn/winter period and the passage of frontal systems in the region. Considering that the Todos os Santos Bay entrance is practically aligned with the west-east axis, winds from northern and southern quadrants can be considered as down-

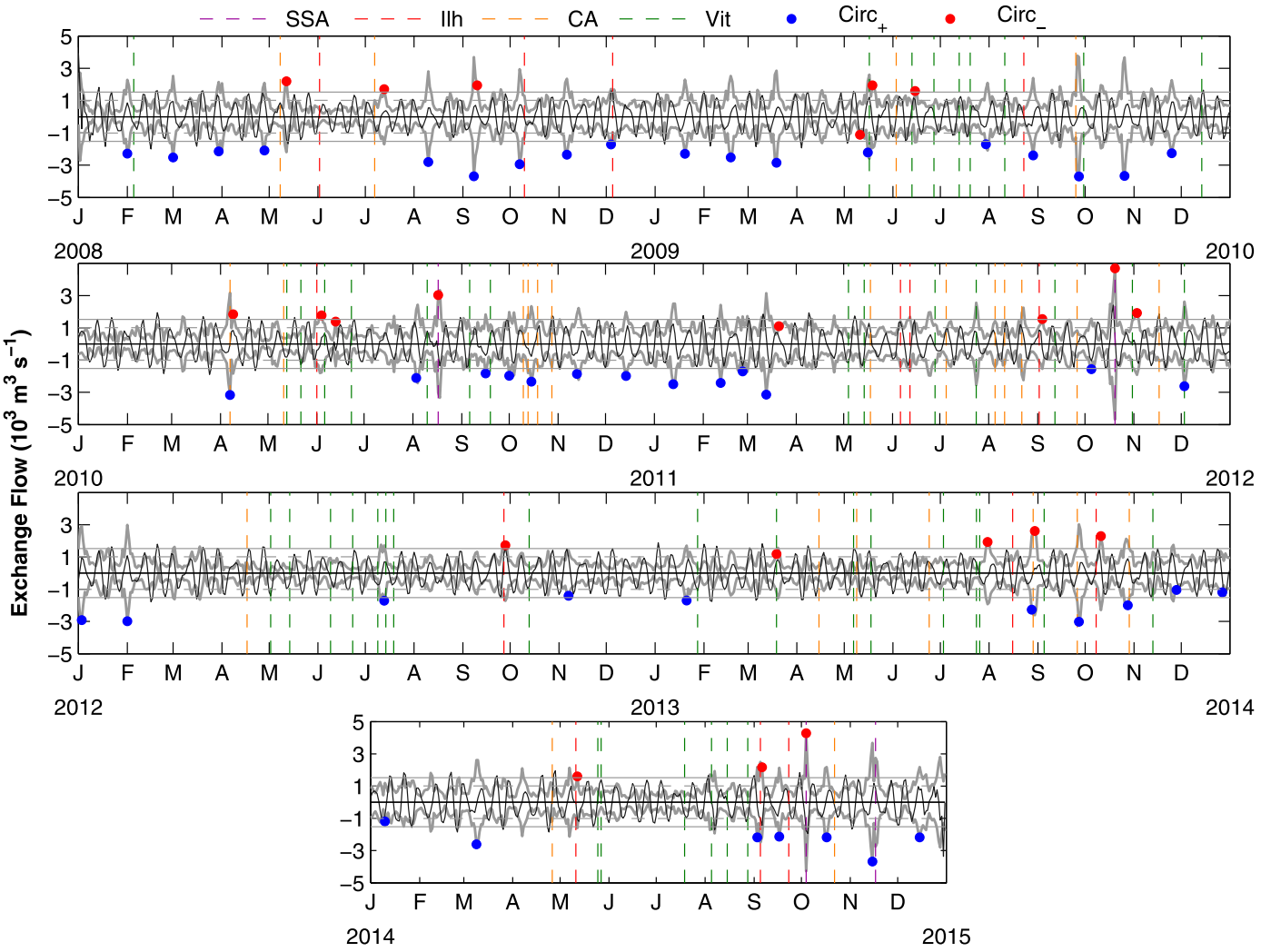

Fig. 5. Time series of components of the exchange flow at the cross-section at the bay entrance (Fig. 1d). Thick gray line indicates Q_{Bi} and solid black line indicates Q_{Uni}. Blue and red circles indicate the peak of $Circ_+$ and $Circ_-$ pulses respectively. The horizontal dashed and solid gray lines indicate 2 and 3 standard deviations of Q_{Bi} respectively. The dashed vertical lines indicate cold front passages at Salvador (13° S, purple), Ilhéus (15° S, red), Caravelas (18° S, orange), and Vitória (21° S, green) recorded by INPE meteorological stations (INPE, 2017), as indicated in Fig. 1b. The units are $m^3 s^{-1}$. (For interpretation of the references to color in this figure legend, the reader is referred to the web version of this article).

estuary and up-estuary winds respectively. Thus, down-estuary winds were predominant during $Circ_+$ pulses, while up-estuary winds were more frequent during $Circ_-$ pulses. Moreover, Fig. 6e and f demonstrate that the more aligned to the along-channel axis the direction of the wind is and the higher the magnitude and frequency of the strongest winds, the stronger the pulses. This is in good agreement with Feng and Li (2010), who suggest that wind direction is an important component in determining the flushing rate.

Table 2 indicates that Q_{Uni} is more related to the intensity of both $Circ_+$ and $Circ_-$ exchange pulses. The total volume of exchange flow and Q_{Bi}, however, depend more on pulse duration and spring tides than on pulse intensity. The total volume of exchange flow also exhibits higher values during $Circ_-$ pulses. All $Circ_+$ and most of $Circ_-$ pulses occurred during neap tides, while about 23% of $Circ_-$ pulses occurred during spring tides. This finding suggests that subinertial forcings may be most influential to the exchange dynamics during neap tides. The amount of total volume exchange appears to increase by the passage of frontal systems. For instance, the greatest total volume exchange occurred when cold fronts were most frequent, mainly in Ilhéus (14.8°S), during $Circ\_std_1$ pulses. This result agrees with Feng and Li (2010), who reported the influence of cold fronts in the total volume transport in Louisiana bays. Cold front passage and changes in wind direction to southwesterly (up-estuary) occurred more often during $Circ_-$ pulses. Nevertheless, cold fronts also occurred during $Circ_+$ related to the intensification of the down-estuary winds prior to their reversal into up-estuary winds. During cold fronts, Feng and Li (2010) observed that pre-frontal winds abruptly reversed and intensified with the approaching of a frontal system. The closer to Todos os Santos Bay cold fronts were recorded, the more intense the $Circ_-$ pulse.

Qualitative and quantitative analyses explored the general features of the exchange pulses identified according to the criteria described in Section 2.2, as follows. Fig. 7a shows that Q_{Bi} is greater than Q_{Uni} during all $Circ_+$ pulses and almost all $Circ_-$ pulses. Furthermore, all $Circ_+$ pulses occurred under stratification conditions, while most (about 60%) of $Circ_-$ pulses occurred in the absence of stratification. Dynamically, all exchange pulses occurred under $Ek < 1$, i.e., under reduced friction. All $Circ_-$ pulses occurred under $Ke > 1$, while approximately 25% of $Circ_+$ pulses occurred under $Ke < 1$. During $Circ_+$ pulses, the stratification possibly increased the internal radius of deformation to a point it became larger than the basin's width, causing the Earth's rotation effect to be less important and the circulation to be vertically sheared.

Regarding the relative importance between the wind stress and baroclinic pressure gradient force, Wn reveals that baroclinicity prevails during most $Circ_+$ pulses while wind stress is most prominent during all

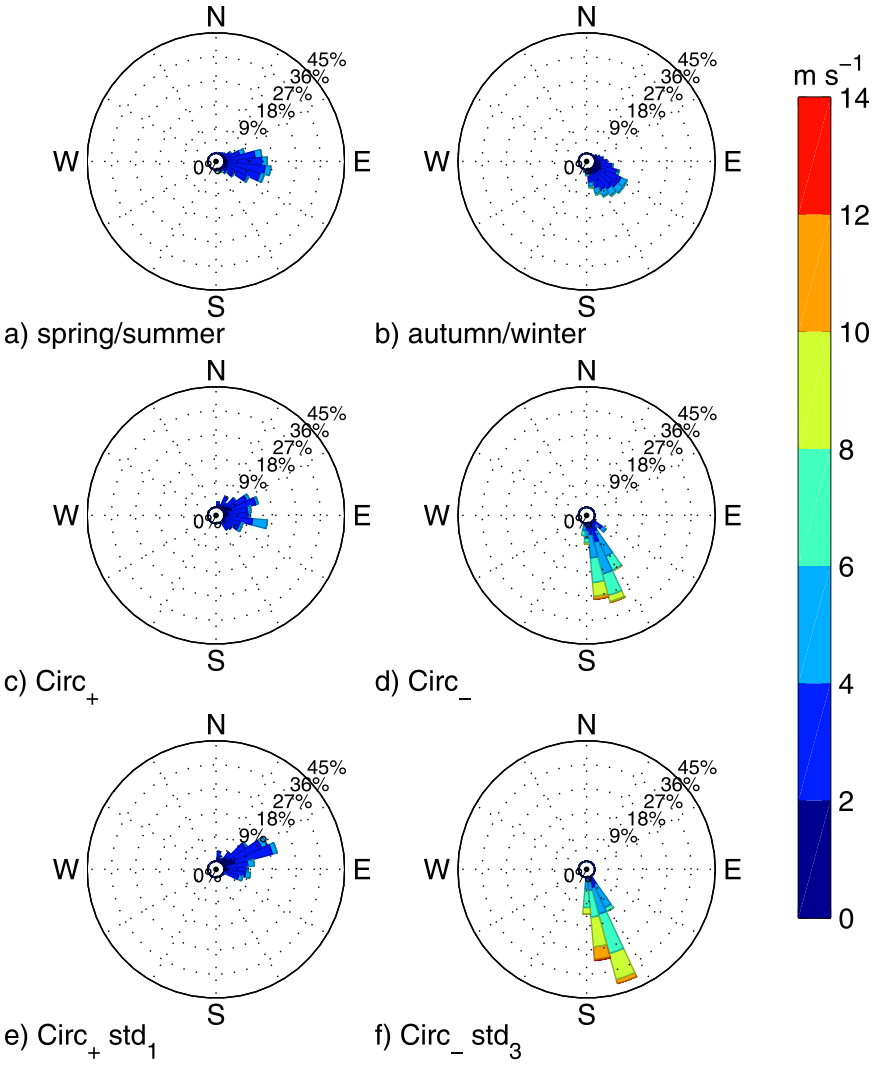

Fig. 6. Wind roses for wind data (CFSR) from 2008 to 2014 within the bay over the water surface during a) spring and summer, b) autumn and winter, c) $Circ_+$ pulse peaks, d) $Circ_-$ pulse peaks, e) $Circ_+std_1$ pulse peaks, and f) $Circ\_std_3$ pulse peaks.

$Circ_-$ pulses. Fr_0 indicates tidal stress as the main mechanism to force total exchange flow during all $Circ_+$ pulses. During 28% of $Circ_-$ pulses, wind stress dominated over tidal stress ($S_0 < 1$) and baroclinicity ($Wn > 1$). Thus, the total exchange flow was mainly wind driven during 6 $Circ_-$ pulses, which represents a shift compared to the mean exchange flow ($S_0 > 1$; $Wn < 1$, Fig. 4a). Quantitative implications are considered next.

Fig. 7b illustrates how the intensity of exchange pulses affects the dynamics at the bay entrance. The stronger and more aligned to the along-channel axis the wind is, the more intense the pulse (Fig. 6). Thus, to understand the exchange pulses, we must also consider the wind's role on stratification, namely wind straining and wind mixing (e.g., Scully et al., 2005; Chen and Sanford, 2009). Table 3 shows that the stronger the $Circ_+$ pulses, the lower Ri. Therefore, even though increased wind mixing decreased Ri, mixing could not overcome wind straining and baroclinic pressure gradient, maintaining stratification. This scenario is in accordance with Scully et al. (2005) and Chen and Sanford's (2009) results, which demonstrated an increase in stratification and exchange flow during moderate down-estuary winds. On the other hand, no pattern was identified with $Circ_-$ intensity and Richardson number (Fig. 7b), despite the expectation of up-estuary winds to reduce stratification (Scully et al., 2005; Chen and Sanford, 2009; Li

Table 2
Number and duration (days) of; total (Q_{Total}), unidirectional (Q_{Uni}) and bidirectional (Q_{Bi}) exchange flow in percentage of volume (%); tides; and cold front (CF) passages (INPE, 2017) during exchange pulses according to their intensities. Percentage of volume is the ratio between volume transport and bay volume in the model ($11.6\ 10^9\ m^3$). The abbreviations indicate the following cities: Salvador (SSA), Ilhéus (Ilh), Caravelas (CA) and Vitória (Vit), as indicated in Fig. 1b.

	std	N	Duration (days)	Q_{Total} (%)	Q_{Uni} (%)	Q_{Bi} (%)	Spring	Neap	CF	CF site
$Circ_+$	0	22	3.4 ± 1.4	−5.0 ± 2.4	0.2 ± 0.8	5.0 ± 2.2	0	22	4	CA
	1	26	4.0 ± 1.3	−4.7 ± 4.7	1.1 ± 1.3	4.9 ± 1.7	0	26	3	CA(1) Vit(2)
$Circ_-$	0	2	4.0 ± 1.4	6.8 ± 16.1	1.1 ± 0.6	3.4 ± 0.5	1	1	1	Vit
	1	8	7.8 ± 4.1	8.0 ± 8.3	0.2 ± 1.4	5.4 ± 2.4	3	5	5	Ilh(4) CA(1)
	2	7	5.7 ± 4.2	3.4 ± 12.3	−0.1 ± 1.4	4.9 ± 2.3	0	7	2	Ilh(1) CA(1)
	3	5	2.8 ± 0.8	−6.3 ± 2.9	−0.9 ± 1.7	5.1 ± 1.5	1	4	4	SSA(3) Ilh(1)

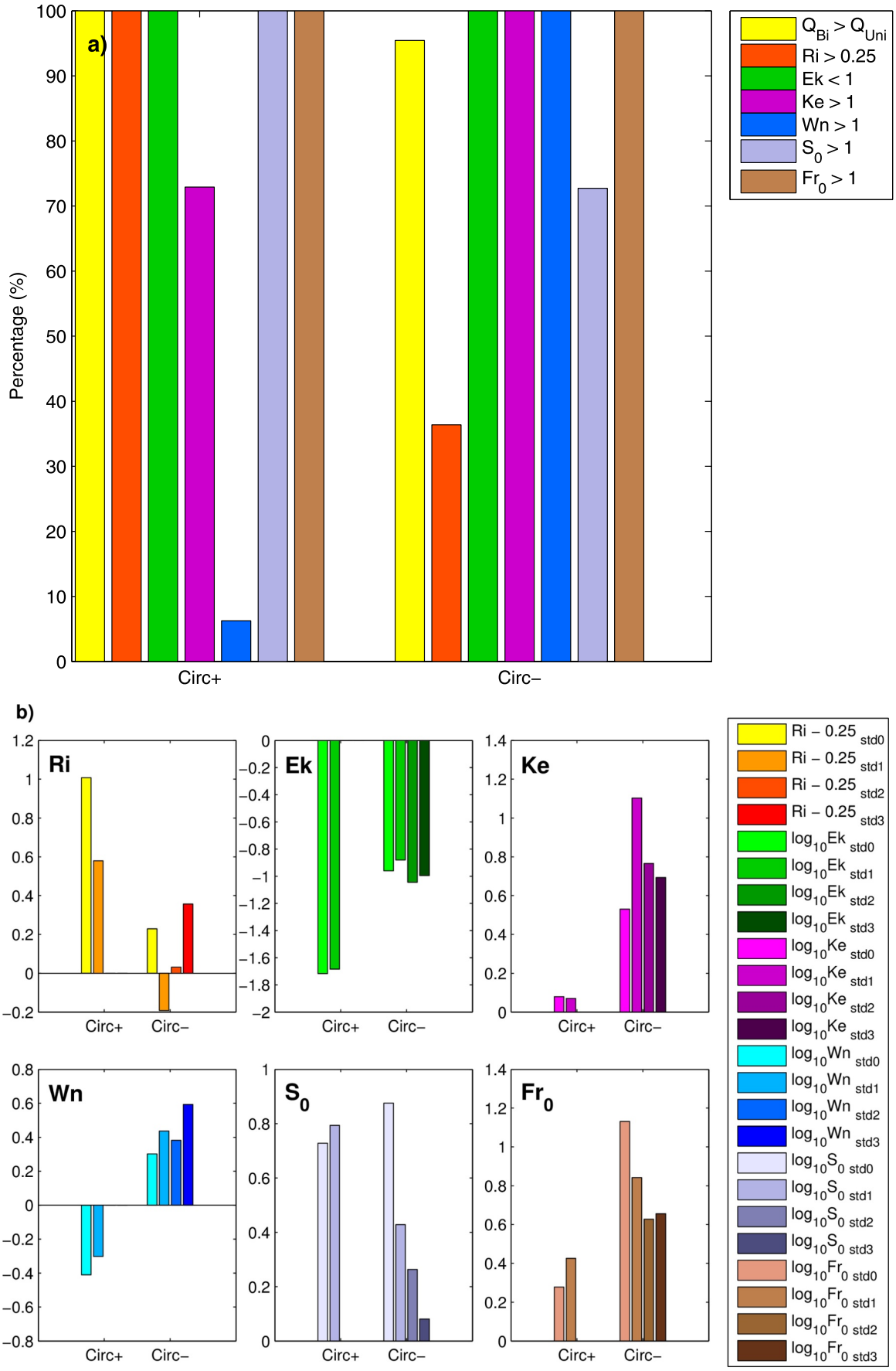

Fig. 7. a) Qualitative analysis: prevailing exchange flow (unidirectional or bidirectional) and nondimensional numbers during $Circ_+$ and $Circ_-$ pulse peaks. b) Quantitative analysis: nondimensional numbers according to the intensity of $Circ_+$ and $Circ_-$ pulse peaks. Nondimensional numbers are evaluated based on the statistical distribution of the events.

Table 3
Mean and standard deviation of the nondimensional numbers during the whole period and exchange pulses according to their intensities.

	std	Richardson (Ri)	Ekman (Ek)	Kelvin (Ke)	Wedderburn (Wn)	Stress ratio (S_0)	Tidal Froude (Fr_0)
Whole period	–	0.18 ± 0.27	0.11 ± 0.05	3.74 ± 4.03	0.70 ± 0.91	20.15 ± 12.59	10.28 ± 11.27
$Circ_+$	0	1.04 ± 0.49	0.02 ± 0.01	1.21 ± 0.32	0.42 ± 0.25	6.50 ± 3.19	2.31 ± 0.88
	1	0.71 ± 0.23	0.03 ± 0.01	1.25 ± 0.49	0.43 ± 0.23	8.24 ± 3.34	3.20 ± 1.48
$Circ_-$	0	0.29 ± 0.39	0.12 ± 0.06	3.58 ± 0.57	1.38 ± 0.89	13.41 ± 9.36	12.07 ± 2.19
	1	0.06 ± 0.09	0.13 ± 0.04	8.02 ± 12.78	1.55 ± 1.07	9.46 ± 11.52	8.09 ± 4.07
	2	0.10 ± 0.22	0.13 ± 0.04	5.56 ± 3.39	1.82 ± 1.12	10.29 ± 13.23	8.67 ± 5.23
	3	0.58 ± 1.02	0.11 ± 0.05	5.10 ± 3.94	3.05 ± 1.33	2.22 ± 2.23	5.63 ± 4.32

and Li, 2011). This may be because some $Circ_-$ were preceded by $Circ_+$, and $Circ_-$ were not sufficiently strong to break the stratification caused by $Circ_+$.

$Circ_-$ occurred in all four intensity ranks considered, being 1 (50%), 1 (13%), 3 (43%) and 3 (60%) pulses occurring under stratification from std_0 to std_3 intensity levels respectively. Therefore, $Circ_-$ pulses occurred under both stratification and its absence regardless of their intensity. This response is possibly related to the passage of cold fronts. As discussed before, i) the closer the cold front, the stronger $Circ_-$ pulses were and ii) cold fronts tended to intensify down-estuary winds prior to their reversal into up-estuary winds, with wind straining causing stratification before $Circ_-$ pulses. Consequently, as frontal systems approach the bay entrance, $Circ_-$ are likely to occur after an increase in stratification.

With respect to the relative importance of rotation, Ek and Ke decreased and increased during $Circ_+$ and $Circ_-$ pulses, respectively, compared to the mean of the entire time series (Table 3). As observed in Fig. 7a, Ke was < 1 during about 25% of $Circ_+$ pulses. Among these pulses, 6 were std_0 and 7 were std_1. Therefore, the internal radius of deformation grew larger than basin's width and along-channel circulation tended to be vertically sheared regardless of the intensity of $Circ_+$ pulses. Wn revealed an increase with pulse intensity regardless of the circulation pattern (Fig. 7b). Wind mixing was enhanced during the strongest $Circ_+$ pulses, but still not overcoming wind straining and baroclinicity. In only three pulses of $Circ_+$, wind mixing prevailed over baroclinic pressure gradient, even though wind straining could still maintain stratification (Fig. 7a). During $Circ_-$ pulses, Wn also increased with pulse intensity, however wind mixing and wind straining worked in concert against the baroclinic pressure gradient to reduce stratification. During only one $Circ\_std_1$ pulse, the baroclinic pressure gradient persisted over wind straining and mixing. This finding is in good agreement with Li and Li (2011) who demonstrated that stratification tends to decrease as Wn increases regardless of either down-estuary or up-estuary winds.

S_0 decreased with $Circ_-$ pulse intensity, although remaining higher than 1. Hence, as more intense $Circ_-$ pulses occurred, the influence of wind stress on the total exchange flow was enhanced, but without overcoming that of tidal stress. No pattern was found concerning pulse intensity and Fr_0.

4. Discussion

We explored the general features of the mean exchange circulation and the exchange pulses in the region. In this section, we investigate the main driver of baroclinicity in Todos os Santos Bay and analyze in more detail each type of exchange pulse, its mechanisms and implications.

4.1. Density gradient force

Correlation coefficients between each fresh water source and the horizontal density gradient were estimated to infer the main forcings of the gravitational circulation (Table 4). The combined discharges of Paraguaçu and Subaé rivers exhibit the highest correlation (0.48). The total discharge of all rivers presents a correlation of 0.42, which underscores the prominent role of Paraguaçu River in inducing the gravitational circulation. Coastal streams and water balance exhibit very low values of correlation. As coastal streams are sparsely distributed within the bay, their diffuse discharges have negligible influence on the horizontal density gradient. A similar situation occurs with the water balance, as precipitation and evaporation affect the entire bay, and no spatial differences in density ensue. Hence, the Paraguaçu River is the main contributor, with Subaé River playing a secondary role, to force the gravitational circulation in Todos os Santos Bay. These results are in good agreement with Santana et al.'s (2018) findings.

Table 4
Correlation coefficients between $\Delta\rho_h$ and fresh water sources.

	Correlation
All rivers	0.42
Paraguaçu and Subaé rivers	0.48
Paraguaçu River	0.47
Subaé River	0.15
Coastal streams	−0.04
Evaporation minus Precipitation (E - P)	0.04

4.2. Along-channel wind effects on gravitational circulation

Recent studies have demonstrated that axial winds can modify estuarine circulation (e.g., Scully et al., 2005; Li and Li, 2011). To understand these modulations in Todos os Santos Bay, one pulse for each circulation pattern ($Circ_+$ and $Circ_-$) was isolated for more in-depth analysis. The effects of both down-estuary and up-estuary winds on gravitational circulation were examined as follows.

4.2.1. $Circ_+$ case - down-estuary wind

One $Circ_+$ pulse occurred from December 2 to 5, 2011, reaching its peak on the 3rd. Down-estuary winds intensified the bidirectional exchange. During this pulse, Q_{Bi} was three times larger than Q_{Uni} (Fig. 8c). As mentioned in Section 2.3, Q_{Bi} can be induced by local wind and/or by horizontal density gradients. Wavelet coherence analyses were performed to investigate which mechanism was responsible for the bidirectional exchange during the pulse (Fig. 8g and h). Wavelet coherence analysis indicated that along-channel wind stress was correlated to Q_{Bi} mainly at periods of 2–5 days. In contrast, $\Delta\rho_h$ was significantly and inversely correlated to Q_{Bi} for periods > 5 days (Fig. 8h). As the horizontal density gradient forces the gravitational circulation, $\Delta\rho_h$ being inversely related to Q_{Bi} is not physically consistent. Hence, the wavelet coherence analysis demonstrates that the along-channel wind stress was the main mechanism driving synoptic exchange flow during the pulse.

During this pulse, locally wind-driven currents forced a vertically sheared volume exchange (Fig. 9f and d respectively). Such tendency of

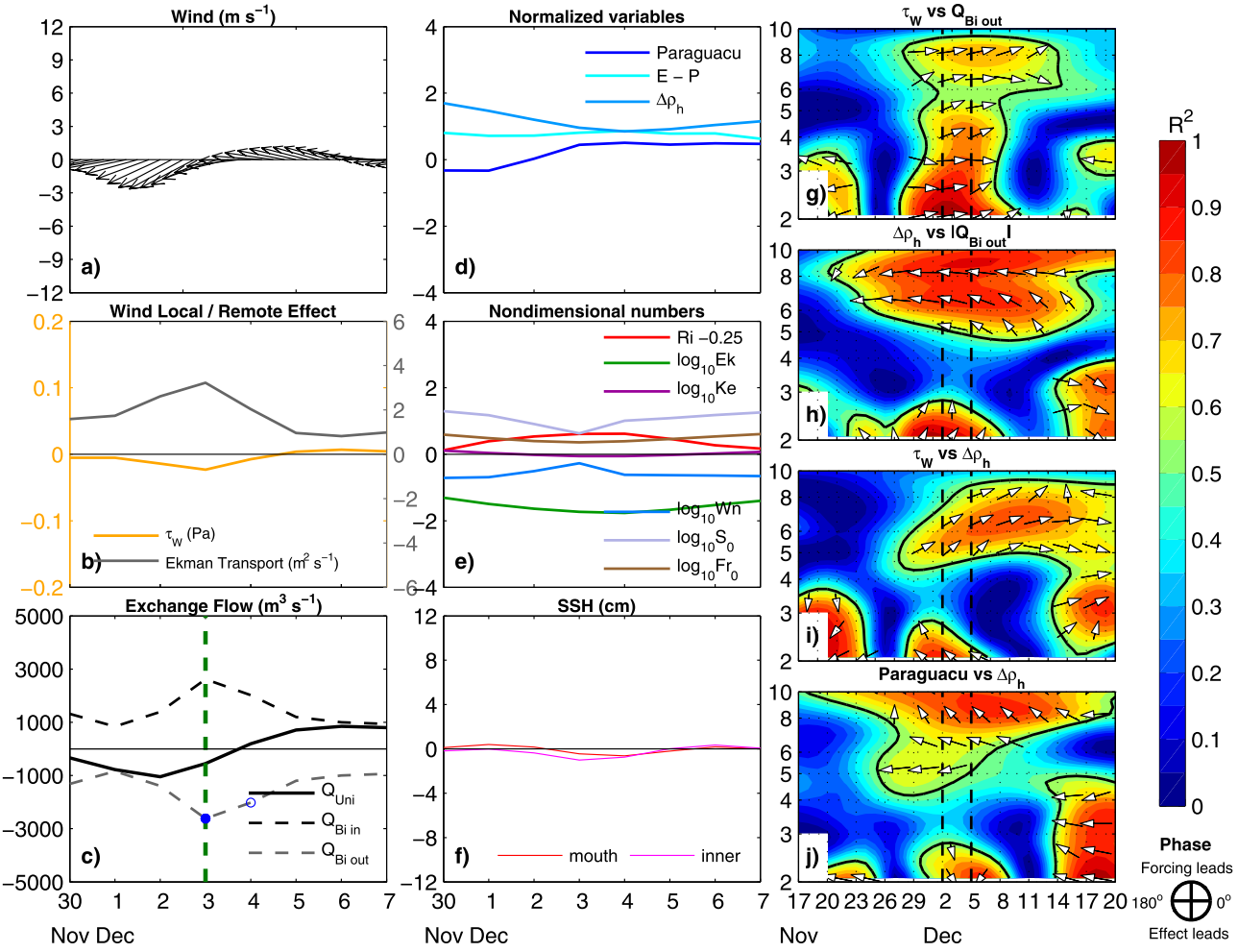

Fig. 8. Time series of a) wind (m s^{-1}) at the midpoint of the cross-section at the bay entrance (Fig. 1d), b) Ekman transport ($m^2 s^{-1}$) and along-channel wind stress (Pa), c) exchange flow ($m^3 s^{-1}$), d) normalized freshwater input and $\Delta\rho_h$, e) nondimensional numbers, f) SSH (cm), and wavelet coherence analysis between g) along-channel wind stress and $Q_{Bi_{out}}$, h) $\Delta\rho_h$ and absolute $Q_{Bi_{out}}$, i) along-channel wind stress and $\Delta\rho_h$, and j) Paraguaçu River discharge and $\Delta\rho_h$ during the $Circ_+$ case pulse. The y-axis for panels g-j indicates the period in days. The black thick line encloses regions with statistical significance at the 95% level of confidence. The white arrows indicate the phase between the time series at a particular period and time according to the scale on the right. (For interpretation of the references to color in this figure, the reader is referred to the web version of this article).

vertically sheared exchange circulation is evidenced by Ke, which is ≪ 1 (Fig. 8e). Although, Todos os Santos Bay is a well-mixed estuary, as discussed in Section 3.2, down-estuary winds induced stratification (Ri > 0.25) during the pulse (Figs. 8e and 9d). Under down-estuary winds, the wind-driven Ekman transport was directed eastward and a clockwise lateral circulation appeared over deep channel. This response is consistent with Li and Li's (2011) findings. These authors also demonstrated that the lateral circulation generated by down-estuary winds steepens isopycnals along the cross-section, while the Coriolis force acting on it decelerates the bidirectional flow, thus reducing the vertical shear.

Both S_0 and Fr_0 were > 1 during the pulse (Fig. 8e). Thus, the total exchange flow remained tidally driven, similarly to the mean exchange flow (Fig. 4a). Regarding the relative importance of wind stress and horizontal density gradient in producing the total ocean-estuary exchange, Wn was clearly increased during the pulse peak, but still small (Wn < 1). This indicates that even though the synoptic exchange flow was mainly wind driven, the total exchange flow remained more density driven than wind driven during the pulse. As Wn depends directly on the wind stress and inversely on the $\Delta\rho_h$, its increase is attributed to two effects: i) intensification of the down-estuary (negative) wind stress and ii) reduction of $\Delta\rho_h$ due to horizontal mixing of the waters along the bay caused by wind during the pulse. These effects become more clear with the aid of wavelet analysis. Fig. 8i suggests that the down-estuary (negative) wind stress is directly (in phase) correlated to $\Delta\rho_h$ during the pulse considering the periods from 5 to 8 days. Thus, as the down-estuary wind stress intensifies (increasingly negative), $\Delta\rho_h$ decreases. During this pulse, even though Fig. 8j shows a significant correlation between Paraguaçu discharge and $\Delta\rho_h$, there is no cause-effect relation as the increase in river discharge is not expected to reduce the horizontal density gradient. Moreover, the horizontal density gradient caused by Paraguaçu River seems restricted to the vicinity of its mouth (Fig. 9b and c). In fact, the Paraguaçu discharge increased while $\Delta\rho_h$ decreased through horizontal wind mixing (Fig. 8i).

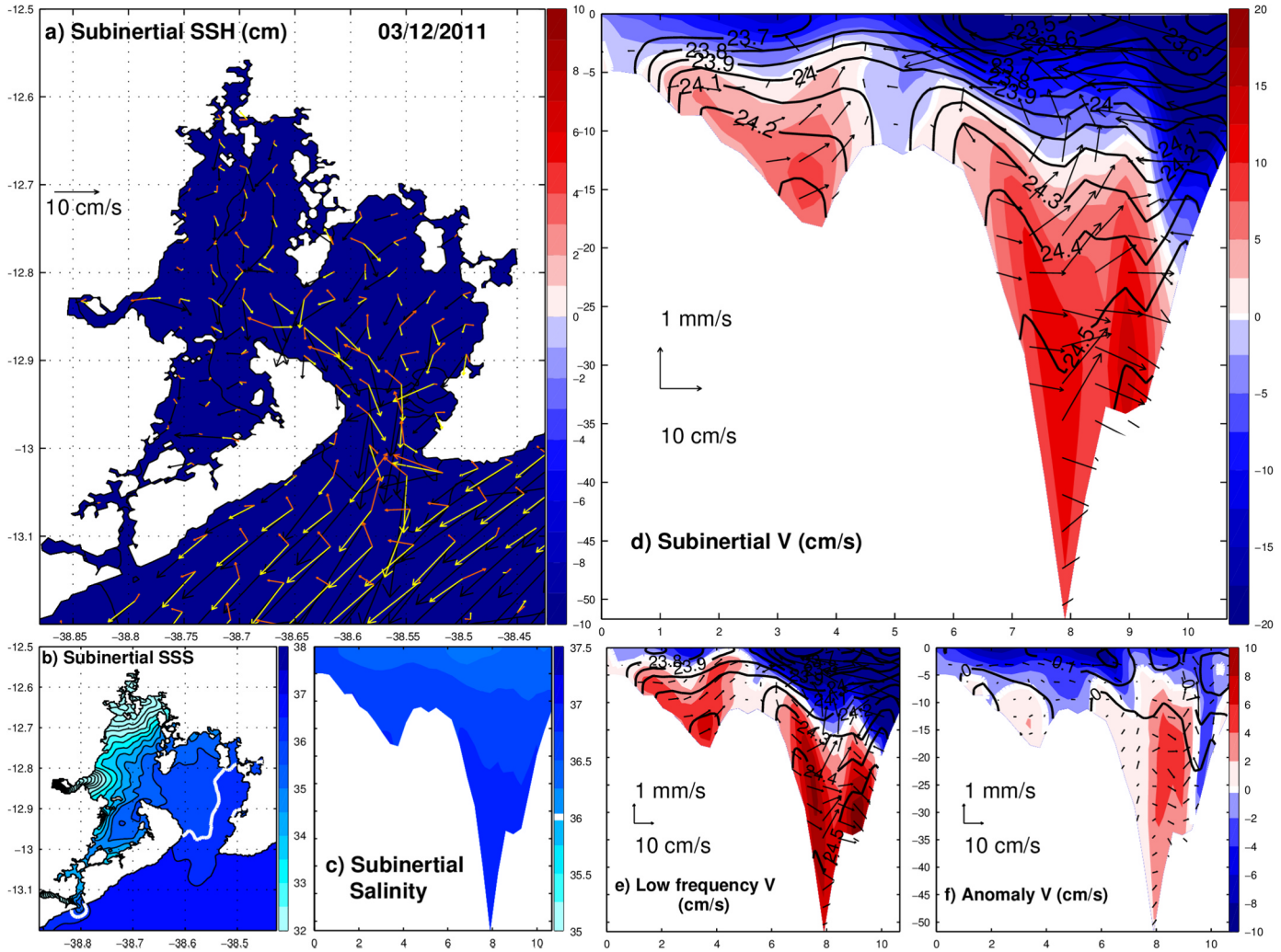

Fig. 9. Maps of a) subinertial SSH (cm) with surface (black), bottom (orange) and net (yellow) current vectors, and b) subinertial surface salinity (SSS) with 36 g kg^{-1} isohaline in white, and profiles of c) subinertial salinity with 36 g kg^{-1} isohaline, d) subinertial, e) low frequency and f) anomaly velocity (cm s^{-1}) with isopycnal contours and lateral circulation vectors during the peak of $Circ_{+}$ case pulse. Positive and negative velocity values indicate inflow and outflow respectively. (For interpretation of the references to color in this figure legend, the reader is referred to the web version of this article).

4.2.2. Circ_ case - up-estuary wind

The strongest $Circ_{-}$ pulse occurred from October 19 to 21, 2011, reaching its peak on the 20th. Analogously to the $Circ_{+}$ case, Q_{Bi} intensified under up-estuary winds (Fig. 10c). With the approach of a frontal system from the south, the wind changed direction and became southeasterly on Dec, 18th, even though the passage of the cold front was recorded in Salvador on Dec, 20th (Fig. 10a). Q_{Bi} was about five times larger than Q_{Uni} during the pulse peak and oscillated with a 4-day period (Fig. 10c). Wavelet analysis shows that the along-channel wind stress was significantly correlated and in phase with $Q_{Bi_{in}}$ from 2 to 4 day period (Fig. 10g). Therefore, Q_{Bi} was prominently driven by the local wind during the pulse.

Both up-estuary along-channel wind stress and onshore Ekman transport were enhanced during the pulse, with the up-estuary wind piling water up toward the bay interior and thus creating an outflow underneath. The sea level difference between bay entrance and inner bay was about 3 cm, at least 3 times greater than that during the $Circ_{+}$ case (Fig. 10f). The onshore Ekman transport, on the other hand, promoted inflow with a 90° phase lag, thus its contribution to the exchange during the peak was practically negligible, similarly to the $Circ_{+}$ case (Fig. 10c). The low frequency exchange (Fig. 11e) resembles the mean circulation during spring tides (Fig. 4b) even occurring during neap tides as the $Circ_{+}$ pulse.

Contours of velocity anomaly show an inverse estuarine circulation: inflow in the surface layer and outflow underneath (Fig. 11f). Although the synoptic exchange flow was vertically sheared, the total exchange flow remained horizontally sheared (Fig. 11d). During the $Circ_{+}$ case, however, the synoptic exchange flow turned the circulation from horizontally to vertically sheared. Why did not this occur during the $Circ_{-}$ case? This seems to be related to the outflow acceleration caused by the interaction of the tidal currents with the St. Antônio Shoal (Fig. 1), also reported by Marta-Almeida et al. (2017). Thus, during $Circ_{+}$, as the intensification of the outflow did not oppose the synoptic exchange flow, the total exchange flow became horizontally sheared. Conversely, the synoptic exchange flow induced inflow at the surface of the channel against the outflow. As the synoptic inflow could not overcome the background outflow, the estuarine exchange remained horizontally sheared. The Earth's rotation effect was relevant (Ke > 1) during the

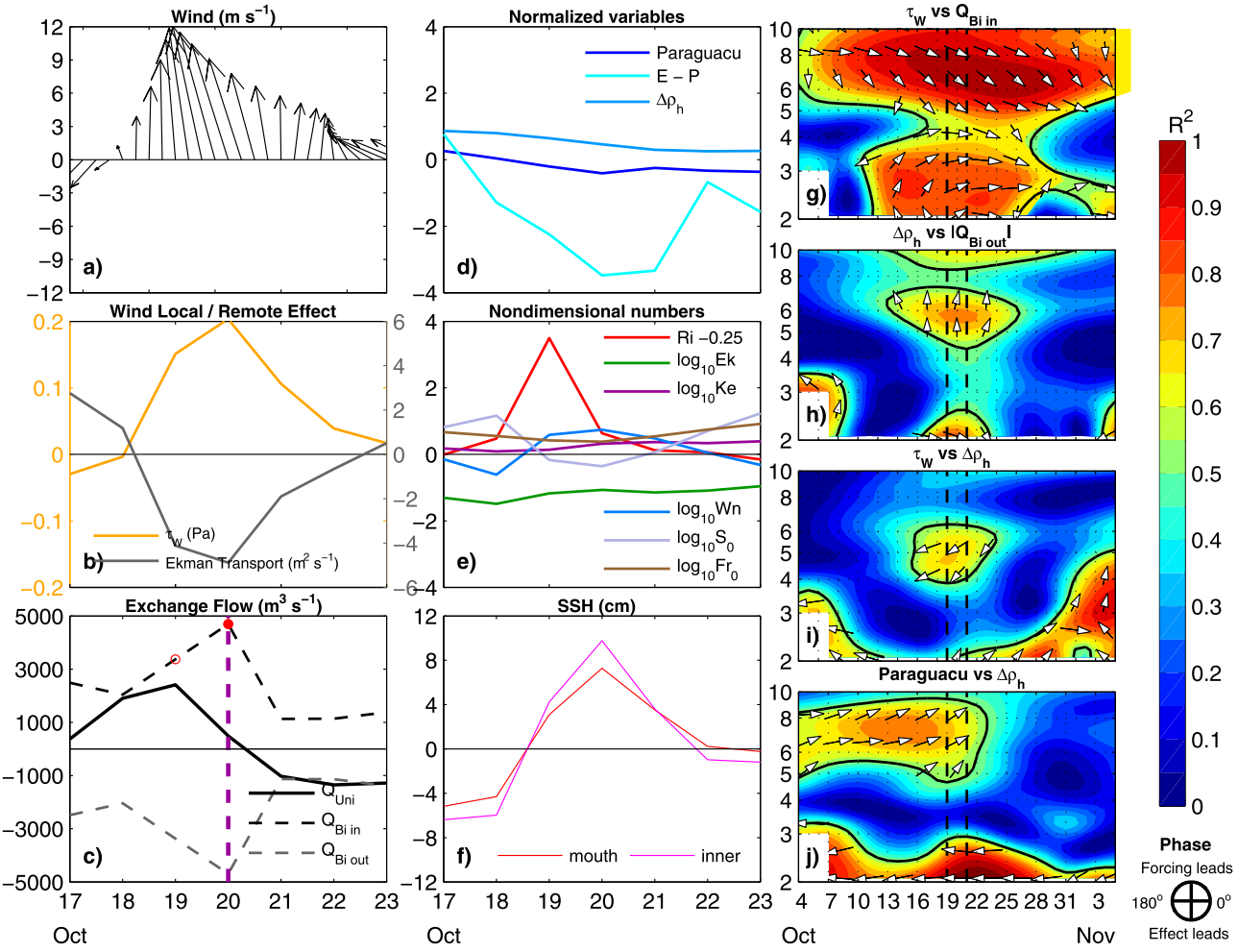

Fig. 10. Time series of a) wind (m s^{-1}) at the midpoint of the cross-section at the bay entrance (Fig. 1d), b) Ekman transport ($m^2 s^{-1}$) and along-channel wind stress (Pa), c) exchange flow ($m^3 s^{-1}$), d) normalized freshwater input and $\Delta\rho_h$, e) nondimensional numbers, f) SSH (cm), and wavelet coherence analysis between g) along-channel wind stress and $Q_{Bi_{out}}$, h) $\Delta\rho_h$ and absolute $Q_{Bi_{out}}$, i) along-channel wind stress and $\Delta\rho_h$, and j) Paraguaçu River discharge and $\Delta\rho_h$ during the *Circ*_ case pulse. The y-axis for panels g-j indicates the period in days. The black thick line encloses regions with statistical significance at the 95% level of confidence. The white arrows indicate the phase between the time series at a particular period and time according to the scale on the right. (For interpretation of the references to color in this figure, the reader is referred to the web version of this article).

*Circ*_ case, which corroborates the tendency of the exchange to be laterally sheared.

The up-estuary wind reduced stratification. This result is consistent with the findings of Scully et al. (2005) and Chen and Sanford (2009). Fig. 10e shows a drastic decrease in Ri during the pulse peak. The preceding stratification peak on Oct, 19th was attributed to rain from the cold front passage, rather than down-wind induced circulation. The Ekman transport driven by up-estuary winds created a counter-clockwise lateral circulation. According to Li and Li (2011), the up-estuary wind-driven lateral circulation flattens cross-channel isopycnals inducing stratification, thus lessening the effects of bottom bathymetry on the flow structure. Noticeably, the lateral circulation generated during the up-estuary wind appears to be stronger than the lateral circulation generated during the down-estuary wind, which is in good agreement with Li and Li (2011). Hence, these similarities with Li and Li's (2011) findings may suggest that lateral circulations generated by both down-estuary and up-estuary winds rearrange isopycnals at the Todos os Santos Bay entrance, reduce the vertical shear in the along-channel bidirectional flow, and the effectiveness of the along-estuary wind straining of the density field. Furthermore, these lateral motions can transport sediment (Geyer et al., 2001; Chen and Sanford, 2009) and also provide an exchange pathway for biologically important materials such as nutrients and oxygen, especially through lateral upwelling and downwelling (Malone et al., 1986; Sanford et al., 1990; Scully, 2010).

Wn for *Circ*_ depicts a different behavior compared to *Circ*+. Wn was higher than 1 when *Circ*_ pattern occurred, indicating that the local wind was more important than baroclinicity during the pulse (Fig. 10e). In addition, S_0 reveals that local wind also dominated over tides ($S_0 <$ 1), and thus the total exchange flow was wind driven during the pulse. In contrast to *Circ*+, wind forced not only the synoptic exchange flow but also the total exchange flow. Nevertheless, the exchange still maintained a laterally sheared pattern. Similarly to *Circ*+, the along-channel wind stress promoted wind mixing horizontally, thus working against $\Delta\rho_h$. Reduction of $\Delta\rho_h$ was also aided by the decreasing of Paraguaçu River discharge.

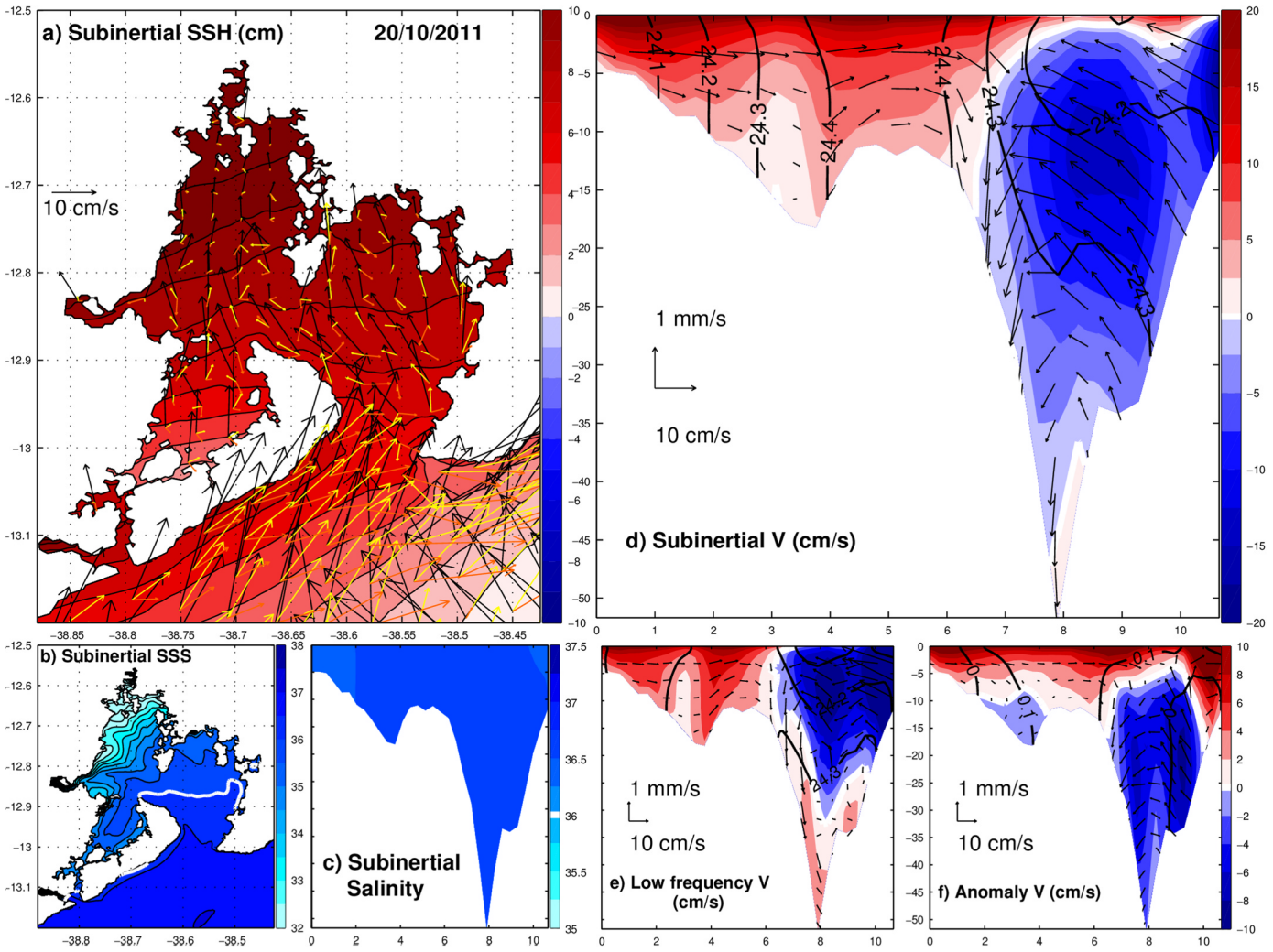

Fig. 11. Maps of a) subinertial SSH (cm) with surface (black), bottom (orange) and net (yellow) current vectors, and b) subinertial surface salinity (SSS) with 36 g kg^{-1} isohaline in white, and profiles of c) subinertial salinity with 36 g kg^{-1} isohaline, d) subinertial, e) low frequency and f) anomaly velocity (cm s^{-1}) with isopycnal contours and lateral circulation vectors during the peak of *Circ_* case pulse. Positive and negative velocity values indicate inflow and outflow respectively. (For interpretation of the references to color in this figure legend, the reader is referred to the web version of this article).

4.3. Connectivity between bay entrance and Jaguaripe River

Despite being part of Todos os Santos Bay catchments, the Jaguaripe River (Fig. 1d) discharges mostly to the shelf. However, Jaguaripe waters can still reach the bay entrance causing connectivity between the river and the bay. We consider connectivity when waters from the Jaguaripe River plume reach the main entrance of the estuary. Fig. 12 demonstrates this connectivity based on four stages: previous, initial, intermediate and peak. On April 10th, 2011, Jaguaripe discharge was about 11 m^{3}s^{-1} and the wind blew south-easterly (Fig. 12a and e). On Apr, 19th, the wind became more aligned with the up-estuary axis and Jaguaripe River discharge increased up to more than 3 standard deviations (Fig. 12b and f). Under such conditions, the Jaguaripe plume was advected toward the bay entrance. As this process developed, less saline waters entered the bay through the western side, generating a marked horizontal density gradient (Fig. 12g). On Apr, 25th, the Jaguaripe plume was advected by up-estuary winds, filling the lower bay with fresher water and decreasing the salinity to less than 36 g kg^{-1} throughout the cross-section (Fig. 12d and h). This connectivity can represent an episodic supply of minerals/nutrients and the migration of species to Todos os Santos Bay.

The internal Rossby radius was estimated at the Itaparica Channel entrance to verify whether rotation also influences the plume dynamics. During all stages, the internal Rossby radius was approximately 2 times larger than the Itaparica Channel basin's width and Ek > 1, thus Earth's rotation effects did not contribute to the northward advection of the plume. Therefore, this case study suggests that the increase in Jaguaripe River discharge in association with up-estuary winds promotes the northward advection of the river plume, which enters the bay and reduces the salinity with a resulting horizontal density gradient on the western side of Todos os Santos Bay entrance.

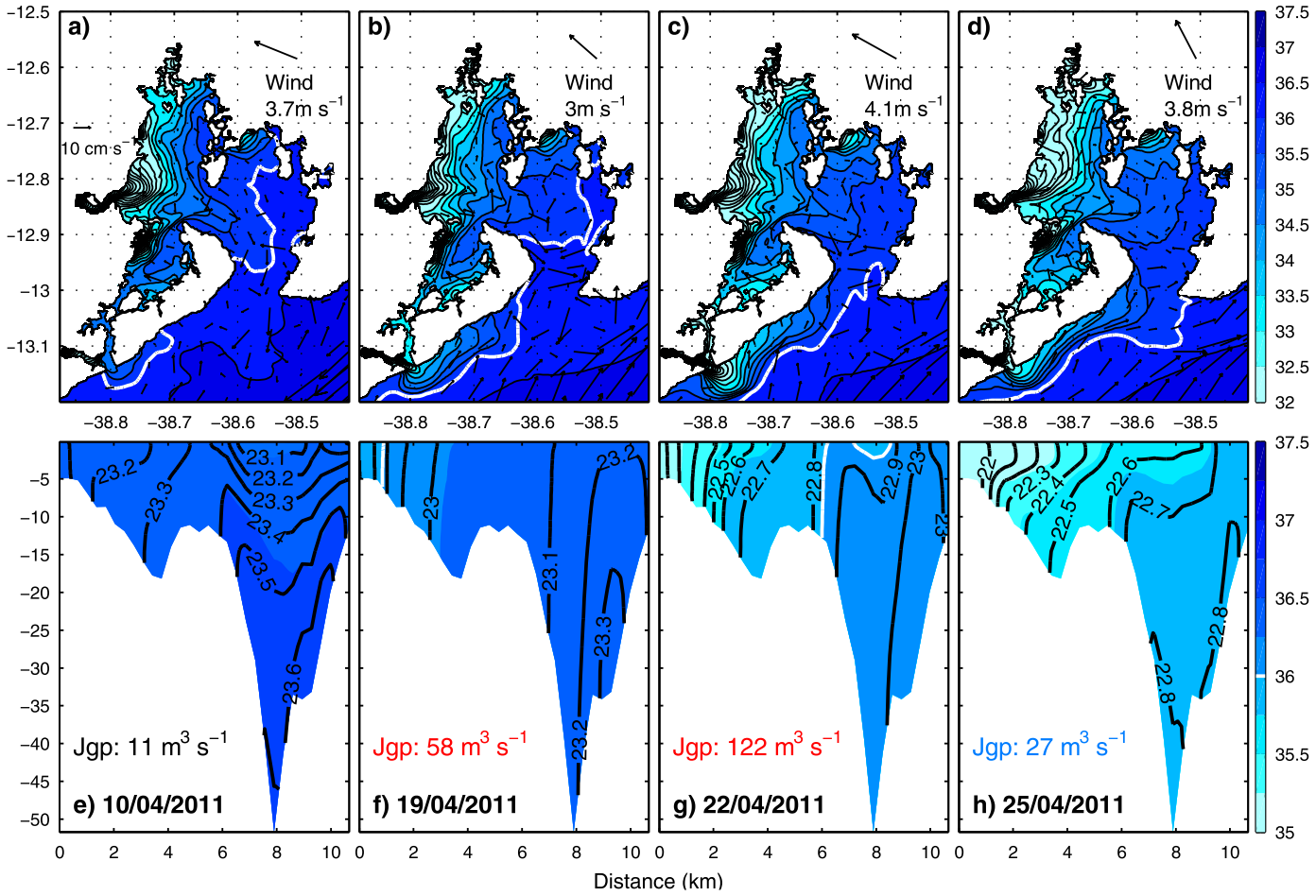

Fig. 12. Upper panels: maps of subinertial surface salinity with surface current vectors during the a) previous stage, b) initial stage, c) intermediate stage and d) peak stage of the Jaguaripe-bay connectivity event. Wind direction and velocity at the midpoint of the cross-section at the bay entrance (Fig. 1d) are presented. Lower panels: subinertial salinity distribution at the cross-section at the bay entrance (Fig. 1d) with isopycnal contours during the e) previous stage, f) initial stage, g) intermediate stage and h) peak stage of the Jaguaripe-bay connectivity event. The interval between isohalines is 0.5 g kg^{-1}. The white thick line indicates the 36 g kg^{-1} isohaline. Jaguaripe River (Jgp) discharge values are presented. Blue and red refers to dischage values between 1 and 2 standard deviations, and above 3 standard deviations respectively. (For interpretation of the references to color in this figure legend, the reader is referred to the web version of this article).

5. Conclusions

High-resolution regional model outputs of a period covering 7 years (2008–2014) were used to study the exchange processes at the Todos os Santos Bay (centered at 13°S). Our results revealed that the mean gravitational circulation consists of a laterally sheared circulation, with outflow constrained by the internal radius of deformation in the surface layer and inflow underneath and over the shoal. Spring and neap tides influence the mean structure of the gravitational circulation: i) reducing and enhancing stratification, and ii) shortening and enlarging the internal radius of deformation, thus forcing the exchange to be more horizontally and vertically sheared respectively. Nondimensional analysis indicated that rotational effects are important and prevail over frictional effects regardless of the tides (low Ekman number). Moreover, this analysis revealed that tidal stress dominates over baroclinic pressure gradient force, which in turn dominates over wind stress, to drive the mean exchange flow.

Analysis of fluctuating exchange pulses indicated that bidirectional rather than unidirectional flow tend to occur regardless of $Circ_+$ (intensification of gravitational circulation) or $Circ_-$ (attenuation/reversal of gravitational circulation). During $Circ_+$, stratification increased as well as the tendency of vertically sheared exchange flow, while during $Circ_-$ this scenario was reversed. Some $Circ_-$ pulses represented a shift in the forcing of the total exchange flow from tidally driven to wind driven.

Detailed analysis in case studies, demonstrated that exchange pulses were wind driven rather than density driven. Down-wind flow developed at the surface and up-wind flow appeared underneath. In addition, our results showed that down-estuary and up-estuary winds induced clockwise and counterclockwise lateral circulation in the vertical plain, which rearranged isopycnals more than along-estuary wind straining at the bay entrance.

Although Jaguaripe River mostly discharges toward the open ocean, up-estuary winds in conjunction with an increase in river discharge promoted northward advection of the river plume. Plume waters reached the main entrance of the estuary, thus generating a horizontal density gradient over the western shoal. This connectivity can represent an episodic supply of minerals/nutrients and the migration of species to Todos os Santos Bay.

This study demonstrated that even though Todos os Santos Bay is located at a low latitude (13°S), its depth and basin's width reveals that Earth's rotation effects must be considered. Our results suggest that findings about estuarine circulation at higher latitudes are applicable at low latitudes when nondimensional analysis indicates that Coriolis effect is important. More in-depth investigation of the connectivity processes involving the advection of the Jaguaripe River plume toward the main entrance is suggested for future work. Further work is also needed to test this study's findings with field observations in order to achieve a better understanding of the estuarine dynamics in the region.

Acknowledgements

This research was supported by PETROBRAS and approved by the Brazilian oil regulatory agency ANP (Agência Nacional de Petróleo, Gás Natural e Biocombustíveis), under the special participation Oceanographic Modeling and Observation Network (REMO) research project. Mauro Cirano and Alessandro L. Aguiar were supported by a CNPq research grant and a CAPES scholarship respectively. Model validation used field data obtained under Projeto FAPESB/Kirimurê. We thank Jean Feingold for proofreading this manuscript. We also thank the two anonymous reviewers for their thoughtful comments.

References

Aguiar, A.L., Cirano, M., Marta-Almeida, M., Lessa, G.C., Valle-Levinson, A., 2018. Upwelling processes along South Equatorial Current bifurcation region and Salvador Canyon (13° S), Brazil. Cont. Shelf Res. 171, 77–96. https://doi.org/10.1016/j.csr.2018.10.001.

Aguiar, A.L., Cirano, M., Pereira, J., Marta-Almeida, M., 2014. Upwelling processes along a western boundary current in the Abrolhos-Campos region of Brazil. Cont. Shelf Res. 85, 42–59. https://doi.org/10.1016/j.csr.2014.04.013.

Amante, C., Eakins, B.W., 2009. ETOPO1 1 Arc-Minute Global Relief Model: Procedures, Data Sources and Analysis. NOAA Technical Memorandum NESDIS NGDC-24, National Geophysical Data Center, NOAA, http://dx.doi.org/10.7289/V5C8276M.

Amorim, F.N., Cirano, M., Marta-Almeida, M., Middleton, J., Campos, E.J.D., 2013. The seasonal circulation of the Eastern Brazilian Shelf between 10°S and 16°S: a modelling approach. Cont. Shelf Res. 65, 121–140. https://doi.org/10.1016/j.csr.2013.06.008.

Amorim, F.N., Cirano, M., Soares, I.D., Lentini, C.A.D., 2011. Coastal and shelf circulation in the vicinity of Camamu Bay (14°S), Eastern Brazilian Shelf. Cont. Shelf Res. 31, 108–119. https://doi.org/10.1016/j.csr.2010.11.011.

Chen, S.N., Sanford, L.P., 2009. Axial wind effects on stratification and longitudinal salt transport in an idealized, partially mixed estuary. J. Phys. Oceanogr. 39 (8), 1905–1920. https://doi.org/10.1175/2009JPO4016.1.

Cirano, M., Lessa, G.C., 2007. Oceanographic characteristics of Baía de Todos os Santos. Braz. Rev. Bras. Geof. 25, 363–387.

CRA, 2001. Saneamento ambiental da Baía de Todos os Santos. Modelamento e avaliaç ao ambiental. Desenvolvimento de modelos computacionais de circulaç ao hidrodinâmica, de transporte de contaminantes e de qualidade da água da BTS. Prognóstico dos efeitos do Programa Bahia Azul com relaç ao à balneabilidade das praias. Tech. Rep. RT-257-05-MA-003-RF, Centro de Recursos Ambientais, Salvador, Bahia, Brazil, 262 pp.

da Silva, A., Young, A.C., Levitus, S., 1994. Atlas of surface marine data 1994, 851 volume 1: Algorithms and procedures. NOAA Atlas NESDIS 6, U.S. Department 852 of Commerce, Washington, D.C.

Dominguez, J.M.L., 2006. The coastal zone of Brazil – an overview. J. Coast. Res. 39, 16–20.

Egbert, G.D., Erofeeva, S.Y., 2002. Efficient inverse modeling of barotropic ocean tides. J. Atmos. Ocean. Technol. 19 (2), 183–204.

Feng, Z., Li, C., 2010. Cold-front-induced flushing of the Louisiana Bays. J. Mar. Syst. 82, 252–264.

Friedrichs, C.T., Hamrick, J.M., 1996. Effects of channel geometry on cross sectional variations in along channel velocity in partially stratified estuaries. In: Buoyancy Effects on Coastal and Estuarine Dynamics. Coastal Estuarine Stud. Ser. AGU Washington, D.C.pp. 283–300.

Geyer, W.R., 1997. Influence of wind on dynamics and flushing of shallow estuaries. Estuar. Coast. Shelf Sci. 44, 713–722.

Geyer, W.R., Woodruff, J.D., Traykovski, P., 2001. Sediment transport and trapping in the Hudson River estuary. Estuar. Coasts 24 (5), 670–679. https://doi.org/10.2307/1352875.

Grinsted, A., Moore, J.C., Jevrejeva, S., 2004. Application of the cross wavelet transform and wavelet coherence to geophysical time series. Nonlinear Process. Geophys. 11 (5/6), 561–566. https://doi.org/10.5194/npg-11-561-2004.

Guo, X., Valle-Levinson, A., 2007. Tidal effects on estuarine circulation and outflow plume in the Chesapeake Bay. Cont. Shelf Res. 27, 20–42. https://doi.org/10.1016/j.csr.2006.08.009.

Guo, X., Valle-Levinson, A., 2008. Wind effects on the lateral structure of density-driven circulation in Chesapeake Bay. Cont. Shelf Res. 28, 2450–2471. https://doi.org/10.1016/j.csr.2008.06.008.

Haidvogel, D.B., Arango, H., Budgell, W.P., Cornuelle, B.D., Curchitser, E., Di Lorenzo, E., Fennel, K., Geyer, W.R., Hermman, A.J., Lanerolle, L., Levin, J., McWilliams, J.C., Miller, A.J., Moore, A.M., Powell, T.M., Shchepetkin, A.F., Sherwood, C.R., Signell, R.P., Warner, J.C., Wilkin, J., 2008. Ocean forecasting in terrain-following coordinates: formulation and skill assessment of the Regional Ocean Modeling System. J. Comput. Phys. 227, 3595–3624.

HYCOM, 2011. Consortium for Data Assimilative Modeling - HYCOM + NCODA Global Analysis. Available at: 〈http://www.hycom.org/dataserver/glbanalysis/〉.

Inall, M.E., Nilsen, F., Cottier, F.R., Daae, R., 2015. Shelf/fjord exchange driven by coastal-trapped waves in the Arctic. J. Geophys. Res. Oceans 120, 8283–8303. https://doi.org/10.1002/2015JC011277.

INPE, 2017. Climanálise - boletim de monitoramento e análise climática. Vols. 23 to 29. Available: 〈http://climanalise.cptec.inpe.br/rclimanl/boletim/〉. (Accessed 20 July 2017).

Kasai, A., Hill, E., Fujiwara, T., Simpson, J.H., 2000. Effect of the Earth's rotation on the circulation in regions of freshwater influence. J. Geophys. Res. 105 (C7), 16961–16969.

Lessa, G.C., Cirano, M., Tanajura, C.A.S., Silva, R.R., 2009. Oceanografia física. In: Hatje, V., Andrade, J. (Eds.), Baía de Todos os Santos: Aspectos Oceanográficos. EDUFBA, Brazil, pp. 68–119.

Li, Y., Li, M., 2011. Effects of winds on stratification and circulation in a partially mixed estuary. J. Geophys. Res. 116, C12012. https://doi.org/10.1029/2010JC006893.

Lima, J.A.M., Martins, R.P., Tanajura, C.A.S., Paiva, A.M., Cirano, M., Campos, E.J.D., Soares, I.D., França, G.B., Obino, R.S., Alvarenga, J.B.R., 2013. Design and implementation of the Oceanographic Modeling and Observation Network (REMO) for operational oceanography and ocean forecasting. Rev. Bras. Geof. 31, 209–228.

Malone, T.C., Kemp, W.M., Ducklow, H.W., Boynton, W.R., Tuttle, J.H., Jonas, R.B., 1986. Lateral variation in the production and fate of phytoplankton in a partially stratified estuary. Mar. Ecol. Prog. Ser. 32 (2–3), 149–160. https://doi.org/10.3354/meps032149.

Marques, C., Ferreira, J., Rocha, A., 2006. Singular spectrum analysis and forecasting of hydrological time series. Phys. Chem. Earth ABC 31, 1172–1179. https://doi.org/10.1016/j.pce.2006.02.061.

Marta-Almeida, M., Cirano, M., Soares, C.G., Lessa, G.C., 2017. A numerical tidal stream energy assessment study for Baía de Todos os Santos. Braz. Renew. Energy 107, 271–287. https://doi.org/10.1016/j.renene.2017.01.047.

Marta-Almeida, M., Hetland, R., Zhang, X., 2013. Evaluation of model nesting performance on the Texas-Louisiana continental shelf. J. Geophys. Res 118, 2476–2491. https://doi.org/10.1002/jgrc.20163.

Marta-Almeida, M., Lessa, G.C., Aguiar, A.L., Amorim, F.N., Cirano, M., 2018. Realistical modelling of shelf-estuary regions: a multi-corner configuration for Baía de Todos os Santos. Ocean Dyn (Submitted for publication).

Marta-Almeida, M., Pereira, J., Cirano, M., 2011a. Development of a pilot Brazilian regional operational ocean forecast system, REMO-OOF. J. Oper. Oceanogr. 4 (2), 3–15.

Marta-Almeida, M., Ruiz-Villarreal, M., Otero, P., Cobas, M., Peliz, A., Nolasco, R., Cirano, M., Pereira, J., 2011b. OOFe: a Python engine for automating regional and coastal ocean forecasts. Environ. Model. Softw. 26 (2), 680–682. https://doi.org/10.1016/j.envsoft.2010.11.015.

Monismith, S., 1986. An experimental-study of the upwelling response of stratified reservoirs to surface shear-stress. J. Fluid Mech. 171, 407–439.

Pawlowicz, R., Beardsley, B., Lentz, S., 2002. Harmonic analysis including error estimates in matlab using t-tide. Comput. Geosci. 28, 929–937.

Ponte, A.L., Gutiérrez de Velasco, G., Valle-Levinson, A., Winters, K.B., Winant, C.D., 2012. Wind-driven subinertial circulation inside a semienclosed Bay in the Gulf of California. J. Phys. Oceanogr. 42, 940–955. https://doi.org/10.1175/JPO-D-11-0103.1.

Pritchard, D., 1952. Salinity distribution and circulation in the Chesapeake Bay estuarine system. J. Mar. Res 11 (2), 106–123.

Saha, S., Moorthi, S., Pan, H., Wu, X., Wang, J., Nadiga, S., Tripp, P., Kistler, R., Woollen, J., Behringer, D., Liu, H., Stokes, D., Grumbine, R., Gayno, G., Wang, J., Hou, Y., Chuang, H., Juang, H.H., Sela, J., Iredell, M., Treadon, K.R., Delst, D.P.V., Keyser, D., Derber, J., Ek, M., Meng, J., H. Wei, R.Y., Lord, S., van den Dool, H., Kumar, A., Wang, W., Long, C., Chelliah, M., Xue, Y., Huang, B., Schemm, J., Ebisuzaki, W., Lin, R., Xie, P., Chen, M., Zhou, S., Higgins, W., Zou, C., Liu, Q., Chen, Y., Han, Y., Cucurull, L., Reynolds, R.W., Rutledge, G., Goldberg, M., 2010. The NCEP climate forecast system reanalysis. Bull. Am. Meteorol. Soc. 91, 1015–1057. https://doi.org/10.1175/2010BAMS3001.1.

Sanford, L.P., Sellner, K.G., Breitburg, D.L., 1990. Covariability of dissolved-oxygen with physical processes in the summertime Chesapeake Bay. J. Mar. Res. 48 (3), 567–590.

Santana, R., Teixeira, C., Lessa, G.C., 2018. The impact of different forcing agents on the residual circulation in a Tropical Estuary (Baía de Todos os Santos, Brazil). J. Coast. Res. 34 (3), 544–558.

Scully, M.E., 2010. Wind modulation of dissolved oxygen in Chesapeake Bay. Estuar. Coasts 33 (5), 1164–1175. https://doi.org/10.1007/s12237-010-9319-9.

Scully, M.E., Friedrichs, C.T., Brubaker, J.M., 2005. Control of estuarine stratification and mixing by wind-induced straining of the estuarine density field. Estuaries 28, 321–326.

Shchepetkin, A.F., McWilliams, J.C., 2005. The regional ocean modeling system: a split-explicit, free-surface, topography following coordinates ocean model. Ocean Model. 9, 347–404.

Smeed, D.A., 2004. Exchange through the bab el mandab. Deep-Sea Res. II 51, 455–474.

Smith, R.L., 1968. Upwelling. Oceanogr. Mar. Biol. 6, 11–46.

Tenorio, L., Valle-Levinson, A., Gomez-Valdes, J., 2018. Subtidal hydrodynamics in a tropical lagoon: a dimensionless numbers approach. Estuar. Coast. Shelf Sci 449–459. https://doi.org/10.1016/j.ecss.2017.11.037.

Valle-Levinson, A., 1995. Observations of barotropic and baroclinic exchanges in the lower Chesapeake Bay. Cont. Shelf Res. 15, 1631–1647.

Valle-Levinson, A., 2008. Density-driven exchange flow in terms of the Kelvin and Ekman numbers. J. Geophys. Res. 113, C04001. https://doi.org/10.1029/2007JC004144.

Valle-Levinson, A., Li, C., Royer, T., Atkinson, L., 1998. Flow patterns at the Chesapeake Bay entrance. Cont. Shelf Res. 18 (10), 1157–1177.

Valle-Levinson, A., Reyes, C., Sanay, R., 2003. Effects of bathymetry, friction and Earth's rotation on estuary/ocean exchange. J. Phys. Oceanogr. 33 (11), 2375–2393.

Valle-Levinson, A., Schettini, C.A.F., 2016. Fortnightly switching of residual flow drivers in a tropical semiarid estuary. Estuar. Coast. Shelf Sci. 169, 46–55.

Valle-Levinson, A., Wong, K., Bosley, K., 2001. Observations of the wind-induced exchange at the entrance to Chesapeake Bay. J. Mar. Res. 59 (3), 391–416.

Valle-Levinson, A., Wong, K., Bosley, K., 2002. Effects of the Hurricane Floyd on the exchange at the Chesapeake Bay Entrance. Cont. Shelf Res. 22, 1715–1730.

Wong, K., 1994. On the nature of transverse variability in a coastal plain estuary. J. Geophys. Res. 99 (C7), 14209–14222.

Wong, K., Valle-Levinson, A., 2002. On the relative importance of the remote and local wind effects on the subtidal exchange at the entrance to the Chesapeake Bay. J. Mar. Res. 60, 477–498.

Xavier, A.G., 2002. Análise hidrodinâmica da Baía de Todos os Santos. pp. 222 Ph.D. thesis, Programa de Pós-Graduação em Engenharia, UFRJ.